

RESEARCH ARTICLE **OPEN ACCESS**

Designed Liquid Crystalline Nanoassemblies From Clinically Validated Polyunsaturated Lipids for Combined Antioxidant, Anti-Apoptotic, and Neurotrophic Treatments

 Thelma Akanchise¹  | Fucen Luo¹  | Borislav Angelov²  | Yuru Deng^{3,4} | Angelina Angelova¹ 
¹Université Paris-Saclay, CNRS, Institut Galien Paris-Saclay, Orsay, France | ²Extreme Light Infrastructure ERIC, Prague, Czech Republic | ³Wenzhou Institute, University of Chinese Academy of Sciences, Wenzhou, China | ⁴Wenzhou Yuanpai Biotechnology Co., Ltd, Wenzhou, China

Correspondence: Angelina Angelova (angelina.angelova@universite-paris-saclay.fr)

Received: 14 November 2025 | **Revised:** 25 March 2026 | **Accepted:** 28 March 2026

Keywords: ginkgolide B | ginkgolide C | hexosomes | ionizable omega-6 polyunsaturated lipid | kaempferol | lipid nanoparticles (LNPs) | mitochondrial oxidative stress | multi-target antioxidants | pH-responsive structures | SAXS

ABSTRACT

Neurodegenerative diseases present a significant challenge in modern medicine, largely due to the interplay of oxidative stress, apoptosis, and neuroinflammation. The development of advanced materials capable of simultaneously regulating multiple pathological processes is a critical unmet need. Here, we introduce ionizable pH-responsive lyotropic liquid crystalline nanocarriers as a promising self-assembled materials-based solution for neuroregeneration. We engineered non-lamellar polyunsaturated (DLin-MC3-DMA)-based lipid nanoassemblies with a unique combination of antioxidant, anti-apoptotic, and neurotrophic functionalities. By incorporating a multi-targeted phytochemical blend (quercetin, ginkgolides B and C, and kaempferol), the lipid-based nanomedicines effectively suppress inflammatory mediators (IL-1 β , NF- κ B, and JNK1/2) and stimulate endogenous antioxidant defenses via NRF2/ARE activation. The mechanistic involvement of the mTOR/AKT/BDNF/GSK3 β pathway was examined to assess the in vitro therapeutic potential of the antioxidant-loaded lipid nanoparticles (LNPs). The designed assemblies activate pro-survival (p-AKT/mTOR) and neurotrophic (BDNF) signaling pathways while preserving mitochondrial integrity in a cellular neurodegeneration model. The ionizable nature of DLin-MC3-DMA imparts pH-responsiveness to the LNPs, driving a progressive enrichment of the inverted hexagonal (H_{II}) phase under acidic conditions. This structural transition enables precise intracellular drug release, thereby enhancing therapeutic efficacy. Building on this, LNP-mediated regeneration enables the development of next generation neurotherapeutic platforms by simultaneously targeting oxidative stress, inflammation, and key neurotrophic pathways.

1 | Introduction

Overproduction of reactive oxygen species (ROS), a key characteristic of mitochondrial dysfunction, and neuroinflammation are core pathological signatures of neurodegenerative disorders, contributing to synaptic dysfunction and progressive neuronal loss. The rising prevalence of neurodegenerative disorders, such as Alzheimer's and Parkinson's disease, highlights the urgent

need for innovative material solutions and therapeutic strategies that can address the multifaceted nature of these conditions [1–5]. At the cellular level, a cascade of mutually amplifying events, including mitochondrial dysfunction, oxidative stress, and chronic neuroinflammation, drives progressive neuronal loss and cognitive decline [6–9]. Conventional therapeutic approaches often fail to achieve significant clinical outcomes due to their inability to concurrently modulate these complex and intertwined

This is an open access article under the terms of the [Creative Commons Attribution-NonCommercial](https://creativecommons.org/licenses/by-nc/4.0/) License, which permits use, distribution and reproduction in any medium, provided the original work is properly cited and is not used for commercial purposes.

© 2026 The Author(s). *Advanced Healthcare Materials* published by Wiley-VCH GmbH

pathological pathways [10–17]. Therefore, the design of advanced materials that can intelligently interact with biological systems and deliver multiple therapeutic agents to the site of action represents a promising frontier. Simultaneous regulation of oxidative stress, inflammatory cascades, and neurotrophic signaling would be a promising strategy for neuroregeneration.

Lipid-based nanoparticles (LNPs) have gained prominence as potent nanocarriers for delivering drugs to the central nervous system (CNS), owing to their biocompatibility, tunable drug encapsulation capabilities, and potential for brain targeting. However, achieving efficient intracellular delivery at therapeutic concentrations remains a significant hurdle. To overcome this limitation, we have engineered lyotropic liquid crystalline pH-responsive nanocarriers based on an ionizable polyunsaturated lipid. The advantage of our self-assembled materials lies in the incorporation of the clinically validated DLin-MC3-DMA ionizable lipid, which imparts pH-sensitivity to the nanostructures (Figure 1). Engineered for pH-responsiveness, the LNPs exhibit coexisting cubic and inverted hexagonal phases at physiological pH, with the H_{II} phase becoming the dominant and more ordered population upon acidification to pH 5.0, characteristic of endosomal compartments. This design may facilitate the controlled release of therapeutic cargo. Moreover, we exploited the potential of the ionizable nanocarriers to deliver a multi-target combination of natural compounds with potent antioxidant, anti-inflammatory, and neurotrophic properties. By co-encapsulating quercetin, ginkgolides B and C, and kaempferol, we created multifunctional nanomedicines that can simultaneously inhibit oxidative stress, suppress neuroinflammation, and promote neuronal survival and regeneration.

The primary purpose of the present study is to develop and in vitro validate an advanced nanomedicine platform capable of addressing the multifaceted pathology of neurodegenerative diseases. We consider that conventional treatments have been ineffective because they target single pathways, whereas neurodegeneration is driven by a complex interplay of oxidative stress, neuroinflammation, and apoptotic cell death.

The intricate architecture of our ionizable lipid nanocarriers is central to their therapeutic potential. We engineered these nanoparticles from lyotropic liquid crystalline lipid phases, which are self-assembled, biomimetic structures that provide exceptional stability in excess aqueous medium and high encapsulation efficiency for bioactive phytochemicals. This advanced material design is critical for overcoming the inherent limitations of free antioxidant compounds (e.g., quercetin, kaempferol, ginkgolides B and C), such as poor solubility, rapid metabolic clearance, and hence an inability to reach therapeutic concentrations in the CNS. By taking advantage of the pH-responsive nature of the ionizable DLin lipid, our nanocarriers were designed to be selectively activated within the acidic microenvironments of endolysosomal compartments. Under acidic conditions, DLin becomes protonated ($pK_a \sim 6.45$) [23], driving a pH-dependent structural transition toward the inverted hexagonal (H_{II}) phase [24, 25]. MO served as the structure-forming nonlamellar lipid template for liquid-crystalline phase formation. The core concept is that DLin not only improves the dynamic phase responsiveness of the studied non-lamellar lipid assemblies but may also enhance neuronal biocompatibility [25–31]. In the context of neurodegeneration,

MO-DLin-based LNPs may provide dual benefits by preserving labile antioxidants and enabling efficient intracellular delivery.

It is hypothesized that the pH-responsive, structure-mediated release mechanism ensures efficient delivery of the therapeutic payload into the cytoplasm of neuronal cells, thereby maximizing its impact on intracellular targets while minimizing off-target effects. In this way, we present a paradigm where the omega-6 lipid material DLin itself is not a passive vehicle but an active element in the therapeutic process responding to specific cellular cues, e.g., the acidic microenvironment under neurodegenerative conditions. By this design, we aimed to restore neuronal homeostasis, protect against neuronal damage, and promote a microenvironment favorable to neuroprotection. For this purpose, we investigated the therapeutic potential of LNP-based nanomedicines (MO-DLin-Plu) to modulate various (mTOR/AKT/BDNF/GSK3 β) signaling pathways linked to neuronal survival and mitochondrial dysfunction. Below, we present details about the pH-responsive nanocarriers as multi-target nanoformulations, their structural characterization, and in vitro evaluation that evidences their potential as a prospective soft materials-based platform for the treatment of neurodegenerative diseases.

2 | Results

2.1 | Structure Determination of Liquid-Crystalline Assemblies Involving the Polyunsaturated Ionizable DLin-MC3-DMA Lipid and Ginkgo Biloba Actives

Lipid-based nanoassemblies with non-lamellar structures, specifically cubosomes and hexosomes, were prepared using lyotropic self-assembled mixtures of MO and DLin lipids. The nanoassemblies encapsulated or co-encapsulated actives from *Ginkgo biloba* extract (EGB) (Figure 1C). Among the phytochemicals chosen for targeting the pathological pathways linked with mitochondrial oxidative stress and neuroinflammation [18–28], quercetin (a polyphenolic flavonol) was incorporated into the LNPs for its potent ROS scavenging and Nrf2 activation. Quercetin promotes mitochondrial biogenesis by mitigating oxidative stress and stabilizing mitochondrial membrane potential ($\Delta\Psi_m$). Ginkgolides B and C (as diterpene trilactones) can suppress neuroinflammation, while preserving $\Delta\Psi_m$, attenuating calcium-mediated mitochondrial injury, and inhibiting complex I/III-derived superoxide production by targeting the inflammation-mitochondria axis that exacerbates neuronal death. Kaempferol (a flavanol) complements these effects by neutralizing ROS and activating AMPK/PGC-1 α signaling to enhance mitochondrial biogenesis. Our dual-payload strategy of combining quercetin with ginkgolide B/C or kaempferol in the same LNPs offers multi-target benefits by exploiting membrane-associated radical quenching and anti-inflammatory pathways.

Synchrotron small-angle X-ray scattering (SAXS) experiments were performed to examine the nanostructural organization of the MO-DLin-based LNPs at two pH conditions (7.0 and 5.0) (Figure 2). The pH 5.0 condition allowed us to mimic the acidic microenvironment associated with neurodegenerative conditions, such as those found in inflamed or damaged neural

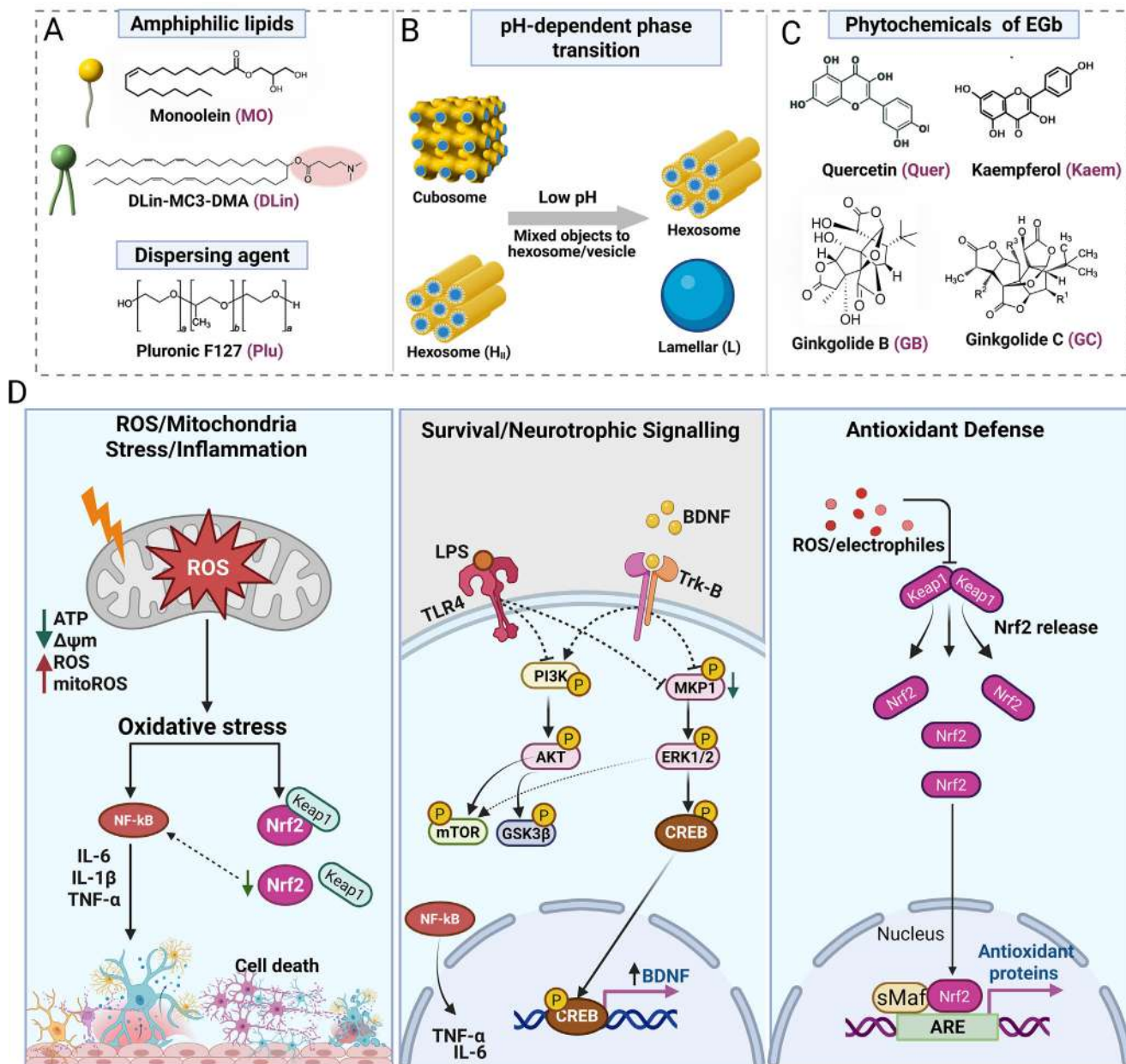


FIGURE 1 | Composition, topology, and action mechanisms of ionizable DLin-MC3-DMA (DLin)-Monolein (MO)-Pluronic F127 (Plu) nanoparticles loaded with multi-targeted antioxidant (quercetin, kaempferol, ginkgolides B and C) actives from *Ginkgo biloba* extract (EGB). (A) Chemical structures of the lipid monolein (MO), the ionizable lipid DLin-MC3-DMA (DLin), and the dispersing agent Pluronic F127 (Plu). (B) Schematic presentation of pH-dependent, DLin-mediated structural transition of MO-DLin-Plu LNPs. Lowering pH transforms the nonlamellar mixture of LNPs into a predominant inverse hexagonal phase (H_{II}). (C) Chemical structures of encapsulated compounds quercetin, kaempferol, and ginkgolides B and C. (D) Schematic representation of mitochondrial oxidative stress, survival/neurotrophic signaling, and antioxidant defense pathways in neuronal cells [18–22]. Mitochondria-derived ROS (mitoROS) trigger oxidative stress, leading to NF-κB activation and release of proinflammatory cytokines (IL-6, IL-1β, TNF-α), while impaired Nrf2 activation contributes to cell death. Moreover, lipopolysaccharide (LPS) stimulation via TLR4 receptors inhibits PI3K/AKT/mTOR and ERK1/2 pathways and therefore modulates GSK3β and CREB activity. These cascades promote or inhibit expression of brain-derived neurotrophic factor (BDNF) and neuronal survival and also intersect with NF-κB-induced inflammatory responses. In parallel, ROS or electrophiles induce Nrf2 dissociation from Keap1, allowing nuclear translocation and binding to antioxidant response elements (ARE) with sMaf proteins, thereby driving transcription of antioxidant enzymes that counteract oxidative damage (created with BioRender).

tissues, and to evaluate the performance of the LNPs [32–35]. The pH-dependent structural behavior of the lipid carriers enabled the selection of stable formulations, which were subsequently tested in a cellular neurodegeneration model to probe neuroinflammatory pathways, including NF-κB, IL-1β, and JNK1/2.

The SAXS patterns acquired at near physiological pH for MO-DLin-Plu, MO-DLin-Plu-GB, MO-DLin-Plu-GC, and MO-DLin-Plu-Quer were assigned to coexisting primitive cubic (*Im*3*m*) and inverted hexagonal (H_{II}) structures (Figure 2A). The incorporation of the ionizable lipid DLin in the mixed assemblies

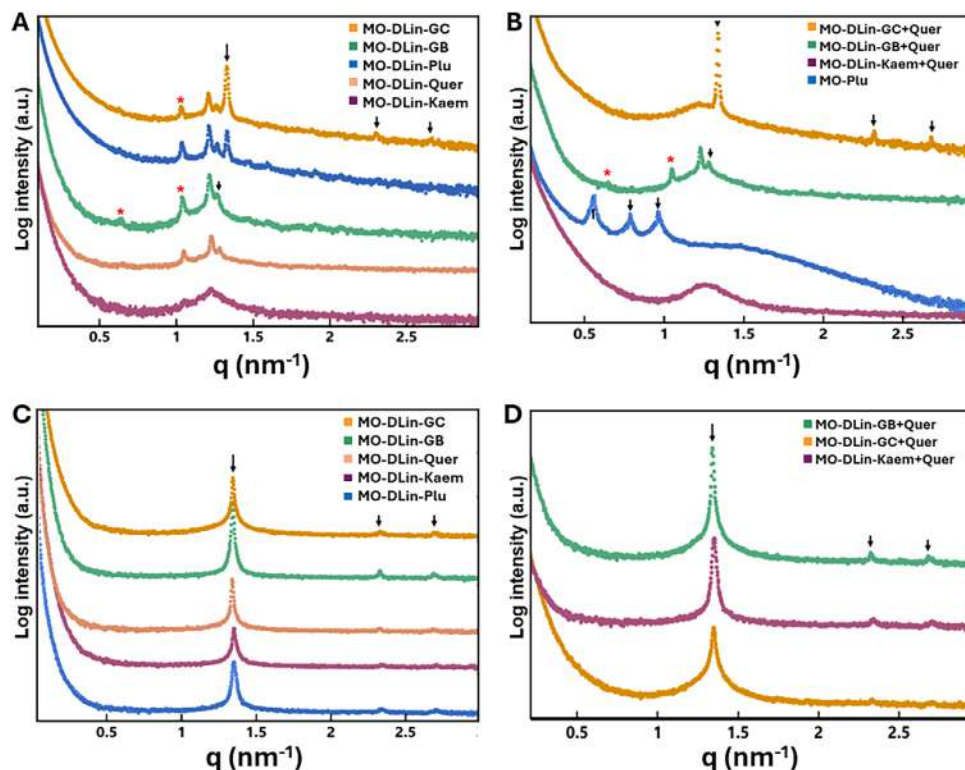


FIGURE 2 | Synchrotron SAXS patterns of MO-DLin-based LNPs at pH 7.0 and pH 5.0. (A and B) SAXS profiles at pH 7.0, showing Bragg peaks of LNPs with an inner inverted hexagonal phase order (hexosomes) coexisting with a weakly ordered $Im3m$ cubic phase. The (10) reflection of the H_{II} phase is occasionally split. The black arrows on the upper patterns indicate the Bragg peak positions indexed by a well-defined H_{II} phase. The red asterisks denote reflections corresponding to minor cubic phase contributions. (C and D) At pH 5.0, the nanoformulations reorganize into a more ordered H_{II} phase. Temperature is 22°C.

significantly impacted the interfacial curvature and mesophase hydration. The main inverted hexagonal H_{II} phase was identified by a strong primary (10) reflection around $q \approx 1.2\text{--}1.3\text{ nm}^{-1}$ and its higher-order reflections, (20) and (21), indicated by black arrows. The dominant H_{II} peak positions for MO-DLin-Plu and MO-DLin-Plu-GC were aligned, with the sequence of Bragg peak maxima positioned at $q_1 = 1.334\text{ nm}^{-1}$, $q_2 = 2.305\text{ nm}^{-1}$, and $q_3 = 2.667\text{ nm}^{-1}$, and unit cell lattice parameter $a_{HII} = 5.45 \pm 0.05\text{ nm}$.

A similar trend was observed for the MO-DLin-Plu-GB and MO-DLin-Plu-Quer nanodispersions, which yielded unit cell lattice parameter $a_{HII} = 5.69 \pm 0.05$ and $5.64 \pm 0.05\text{ nm}$, respectively. A subtle splitting of the first H_{II} reflection (10) was also observed, which can be attributed to incomplete hexagonal phase formation in the amphiphilic mixture or the coexistence of two distinct H_{II} subpopulations. A minor contribution from residual short-range cubic order cannot be excluded. Indeed, a minor contribution from a cubic $Im3m$ phase was observed, indicated by weak reflections at lower q -values (Figure 2A,B, red asterisks), such as the (211) reflection around $q \approx 1.03\text{ nm}^{-1}$. Well-defined characteristic cubic reflections were absent under these conditions of drug loading.

The estimated lattice parameter for the identified $Im3m$ cubic phase of the MO-DLin-Plu, MO-DLin-Plu-GB, MO-DLin-Plu-GC, and MO-DLin-Plu-Quer LNPs corresponded to $a_Q = 13.93, 14.62, 14.14,$ and $14.03 \pm 0.03\text{ nm}$, respectively. In contrast, the

blank MO-Plu formulation lacking a DLin lipid, displayed a well-ordered $Im3m$ cubic structure with distinct q -vector positions at $q_1 = 0.553\text{ nm}^{-1}$, $q_2 = 0.789\text{ nm}^{-1}$, and $q_3 = 0.968\text{ nm}^{-1}$ corresponding to a cubic lattice parameter of $a_{Q(Im3m)} = 15.67 \pm 0.03\text{ nm}$ (Figure 2B, blue plot). The addition of the polyunsaturated lipid DLin appears to dehydrate the cubic phase structure, promoting a higher degree of negative membrane curvature that favors the formation of coexisting hexagonal (H_{II}) phase structures.

Interestingly, the MO-DLin-Plu-Kaem LNPs exhibited a broad, low-intensity peak at $q_1 = 1.221\text{ nm}^{-1}$ assigned to the (10) reflection of a predominantly inverted hexagonal (H_{II}) phase with poorly developed hexagonal-phase domains (Figure 2A, purple plot). The H_{II} phase appears to coexist with a vesicular lamellar fraction. However, upon co-encapsulation of kaempferol or quercetin, the bilayer structure prevailed (Figure 2B, purple plot). For the co-encapsulation of ginkgolide C and quercetin, a well-defined hexagonal phase was resolved with a lattice parameter of $a_{HII} = 5.39 \pm 0.05\text{ nm}$ (Figure 2B, yellow plot).

Next, we evaluated the pH-responsiveness of the MO-DLin LNPs upon acidification of the environment to pH 5.0. Samples initially prepared at pH 7.0 were acidified to pH 5.0 and characterized by SAXS to monitor eventual structural transformations. The SAXS profiles at pH 5.0 for all formulations demonstrated a dominant inverted hexagonal phase formation, revealed by well-defined (10), (11), and (20) Bragg reflections (Figure 2C,D). The

pH shift favoured more negative curvatures, where the weak doublet (10) reflection recorded at near neutral pH merged into a sharper and stronger single Bragg peak of an H_{II} phase at pH 5.0. Upon exposure to an acidic environment, the protonation of DLin's tertiary amine headgroup increases its effective molecular volume and promotes stronger negative curvature. For the MO-Plu LNPs, the predominant cubic phase (cubosomes), originally observed in the lack of DLin, was not sensitive to the pH shift to 5.0. Upon incorporation of the ionizable lipid DLin, the internal nanostructure of the LNPs shifts toward a cubosome/hexosome coexistence, with a higher fraction of the H_{II} phase.

Figure 2C demonstrates the pH-dependent phase transition toward predominantly hexagonal phase structures observed at acidic pH values. Therefore, the ionizable DLin lipid acts as a structural modulator, enhancing the dynamic phase responsiveness of the amphiphilic MO-Plu dispersion. It introduces tunable structural features that respond to changes in the environmental pH. The SAXS results in Figure 2 indicate that the hexosome particles form a growing population at pH 5.0.

Table S1 presents a semi-quantitative phase analysis of the relative liquid crystalline phase contributions at pH 7.0 and pH 5.0. The analysis was performed by integrating the Bragg peak intensity of the assigned inverted hexagonal and cubic $Im3m$ phase reflections. It confirms that the LNP dispersion is essentially enriched in hexosomal-type nanoparticles at pH 5.0.

Figure 3 shows cryo-transmission electron microscopy (Cryo-TEM) images of LNP formulations complementing the reciprocal-space information obtained from SAXS (Figure 2). Cryo-TEM provides direct, real-space evidence about the structural transitions. Hexosome nanoparticles with an inverted hexagonal phase interior dominate the image in Figure 3A. The large hexosome assembly is dispersed into discrete, small hexosome particles. The internal structure of the hexosome particles was resolved at higher magnification (Figure 3B), revealing the distinctive and tightly packed parallel fringes characteristic of hexagonally arranged lipid cylinders viewed from the side (see the inset in Figure 3A). To unequivocally confirm this structure, a Fast Fourier Transform (FFT) was performed on the ordered region (inset, Figure 3B). The resulting pattern shows a six-fold symmetry, providing proof of a liquid crystalline lattice.

At pH 7.0, cryo-TEM revealed particles with complex internal architectures. Figure 3C shows a representative particle, a cubosome, which is the dispersed nanoparticulate form of a bulk cubic liquid crystalline phase. The internal structure displays the characteristic spongy appearance of a cubic phase, with some regions appearing as fragmented polyhedral domains and others showing a more ordered lattice. The FFT of this ordered region (inset, Figure 3C) produced a diffraction pattern consistent with a cubic lattice. The SAXS analysis of the nanodispersions (Figure 2) indicated the presence of a cubic phase as well. Figure 3D shows that a change in the lipid-drug composition at pH 7.0 can hamper the formation of ordered non-lamellar phases, resulting instead in the formation of vesicles coexisting with small hexosomes. These data correlate with the SAXS results (Figure 2A). The topological heterogeneity of the multicomponent LNPs reflects their dynamic structural transformations, which may be critical for the interaction with living cells (described below).

2.2 | In Vitro Biological Evaluation

To link the material properties with the biological effects of the multicomponent pH-responsive LNPs, incorporating quercetin, ginkgolide B, ginkgolide C, and kaempferol, we considered the key pathological characteristics of the neurodegenerative disorders at the cellular level.

Mitochondrial dysfunction has been reported to be the greatest risk factor for neurodegenerative diseases through the accumulation of mitochondrial DNA (mtDNA) mutations and net production of reactive ROS [10, 11, 13, 36]. Excessive ROS and mitochondrial ROS (mitoROS) production reduce ATP generation, collapse mitochondrial membrane potential ($\Delta\Psi_m$), and activate proinflammatory pathways such as nuclear factor-kappa B (NF- κ B), which stimulate cytokine release (IL-1 β , IL-6, TNF- α) [14–17]. These oxidative and inflammatory cascades contribute to synaptic dysfunction, apoptotic signaling, and ultimately neuronal death. On the other hand, the endogenous defense systems, such as the nuclear factor erythroid 2-related factor 2 (Nrf2)/antioxidant response element (ARE) pathway, normally counteract oxidative injury by inducing antioxidant proteins, including HO-1, NQO1, and SOD (Figure 1). Under neurodegenerative conditions, Nrf2 activation is often impaired, which can lead to neuronal damage. In parallel, survival and plasticity pathways involving phosphoinositide 3-kinase (PI3K)/AKT/mTOR/GSK3 β and MAPK/ERK/CREB cascades, as well as BDNF-TrkB signaling, are dysregulated, leading to reduced synaptic plasticity and diminished neurodegenerative processes (Figure 1) [18–22].

Oxidative stress may also activate signaling pathways that alter APP or tau processing in AD pathology. Moreover, oxidative stress may increase the expression of β -secretase through activation of c-Jun amino-terminal kinase and p38 mitogen-activated protein kinase (MAPK), and increase aberrant tau phosphorylation by activation of glycogen synthase kinase 3 [37–39]. Many of the genes associated with PD also implicate mitochondria in disease pathogenesis. So far, mutations or polymorphisms in mtDNA and nuclear genes such as α -synuclein, parkin, *DJ-1*, *PINK1*, *LRRK2*, and *HTRA2* directly or indirectly involving mitochondria have been identified as causing PD [4, 40–42]. These findings motivated our research on the ability of the engineered liquid crystalline nanocarriers with a pH-responsive nature to overcome the challenges of conventional treatments.

2.2.1 | MO-DLin LNPs Antioxidant-Loaded Formulations Attenuate LPS-Induced Mitochondrial Superoxide Production in SH-SY5Y Cells

Mitochondrial damage, particularly to mitochondrial DNA (mtDNA), is a major cause of excess ROS production. Superoxide radicals ($O_2^{\bullet-}$) are among the primary ROS generated in mitochondria. They can be readily detected by MitoSOX Red, a triphenylphosphonium (TPP $^+$)-linked dihydroethidium (DHE) compound that is selectively oxidized by superoxide, resulting in red fluorescence emission. To investigate whether mitochondrial damage led to increased ROS production, differentiated SH-SY5Y cells were treated with lipopolysaccharides (LPS) (1 μ g/mL, 24 h) followed by exposure to MO-DLin LNP

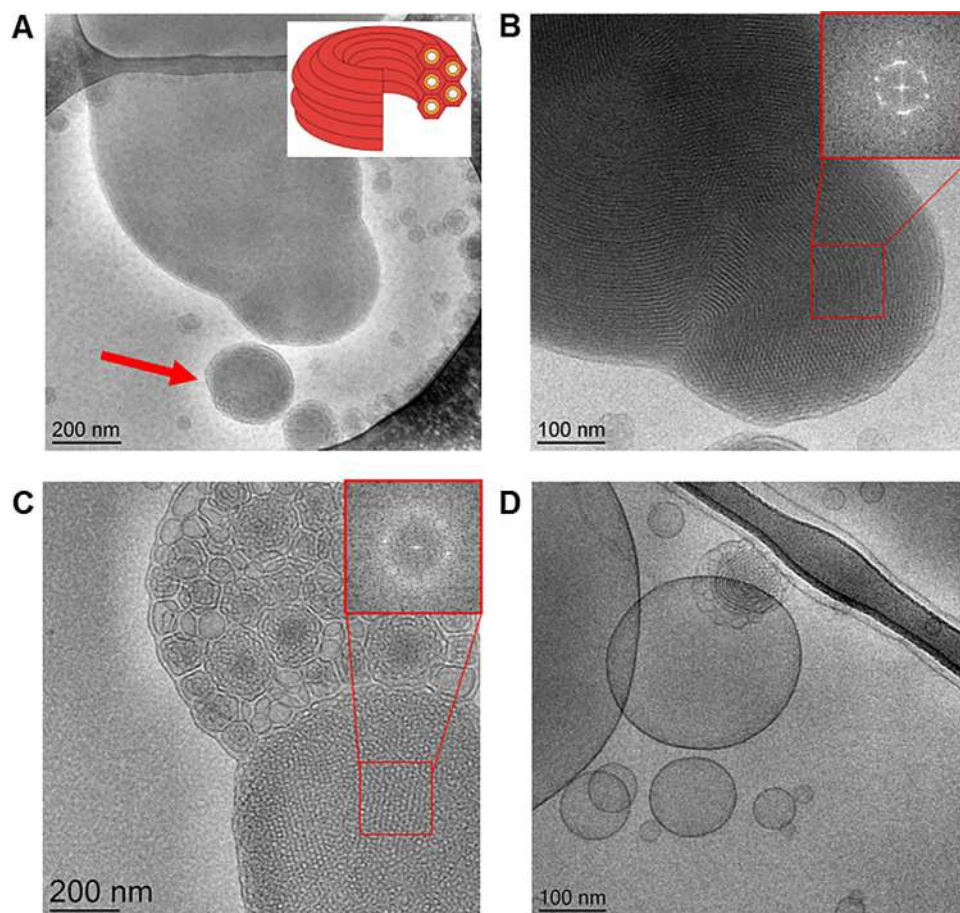


FIGURE 3 | Cryo-TEM images revealing structural transitions of the LNPs sensitive to the environment. (A) Inverted hexagonal phase formulation showing the presence of a large hexosome assembly with an anisotropic shape and a well-formed hexosome particle (indicated by the red arrow). The inset provides a schematic of the internal H_{II} phase structure, consisting of hexagonally packed aqueous channels within a continuous lipid matrix. (B) A high-magnification image of the hexosome LNP. The image reveals the characteristic periodic “fingerprint” pattern, which corresponds to a side-on view of the packed lipid cylinders. The inset Fast Fourier Transform (FFT) of the ordered region displays a distinct six-fold symmetry pattern, providing proof of the hexagonal lattice. (C) Cryo-TEM image of an LNP particle from a formulation at neutral pH (7.0), exhibiting the features of a cubosome. The internal structure shows a more ordered cubic lattice in the lower region and fragmented, polyhedral domains in the upper region. The inset FFT of the ordered domain shows a complex spot pattern consistent with a cubic phase. (D) Coexistence of a small hexosome with vesicles formed in a comparative formulation prepared at a different drug loading. The lack of ordered internal nanostructure in these particles highlights the role of the composition in stabilizing the final particle morphology. Scale bars: 200 nm in (A) and (C); 100 nm in (B) and (D).

series, after which mitochondrial superoxide was assessed using MitoSOX Red staining. Flow cytometry analysis demonstrated that LPS treatment significantly increased MitoSOX fluorescence compared with untreated control cells. This confirmed enhanced mitochondrial ROS production (Figure 4A). Additionally, the selected positive control, 6-hydroxydopamine (6-OHDA), led to an activation of superoxide levels. The comparison indicates that the chosen neurotoxin (LPS) effectively induces mitochondrial ROS production.

Importantly, subsequent treatment with MO-DLin-based nanoformulations revealed varied efficacy in modulating mitochondrial ROS. The majority of LNPs, including MO-DLin-Plu, MO-DLin-Quer, MO-DLin-GB, MO-DLin-GB+Quer, and MO-DLin-Kaem+Quer, decreased mitochondrial superoxide levels compared with the LPS group. In contrast, MO-DLin-GC and MO-DLin-Kaem did not reduce superoxide production, exhibiting profiles similar to those of LPS-treated cells. Quantitative analysis of MitoSOX⁺ cells confirmed these

observations, with most LNP formulations significantly reducing the proportion of superoxide-positive cells (Figure 2B,C). Therefore, treatment with antioxidant-loaded MO-DLin LNPs can effectively attenuate oxidative stress by scavenging superoxide radicals. Another mechanism that can be suggested is the indirectly boosted endogenous antioxidant defenses (e.g., upregulating SOD, catalase, or glutathione systems).

2.3 | Evaluation of Phytochemical-Loaded MO-DLin LNPs' In Vitro Cytotoxicity, Oxidative Stress, and Antioxidant Response

The cellular safety of the MO-DLin nanocarriers alone and of the MO-DLin LNPs encapsulating single or multiple antioxidants was evaluated in neuronally-derived SH-SY5Y cells to determine dosages appropriate for drug treatment. The cell survival rate was higher than 80% at the studied LNP concentrations, except for MO-DLin-GC+Quer, which was slightly lower (77%

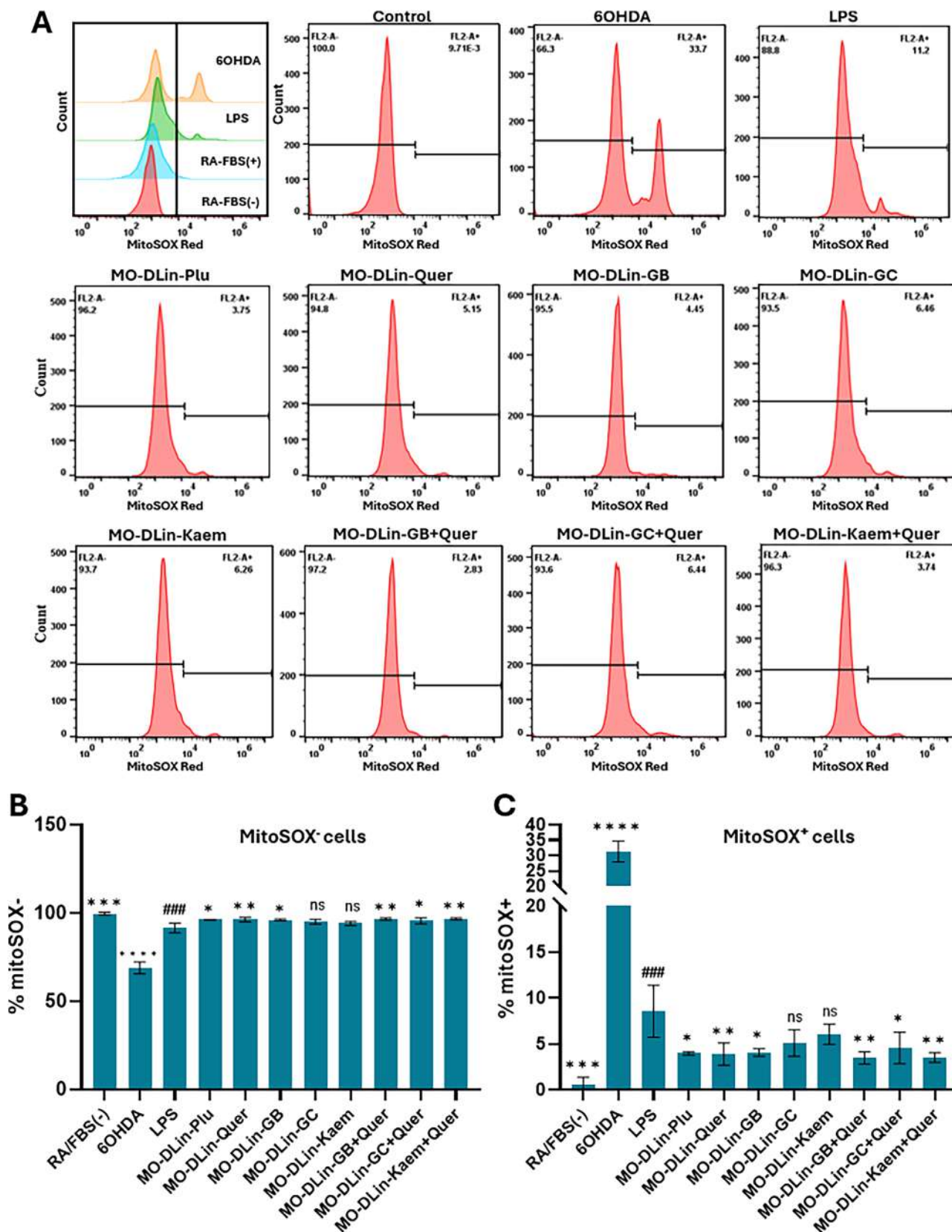


FIGURE 4 | Quantitative analysis of MitoSOX Red fluorescence (% MitoSOX) in LNP-treated differentiated SH-SY5Y cells. (A) Representative flow cytometry histograms are shown for control (no treatment), 6-hydroxydopamine (6-OHDA, positive control), lipopolysaccharide (LPS) induction, and each LNP treatment. Quantitative analysis of (B) relative MitoSOX fluorescence, and (C) percentage of MitoSOX⁺ cells, confirming that LPS significantly increased mitochondrial ROS, whereas most LNP formulations reduced superoxide levels. MO-DLin-GC and MO-DLin-Kaem did not alter ROS levels compared with LPS. Data are presented as mean \pm SD ($n = 3$, * $p < 0.05$, ** $p < 0.01$, *** $p = 0.001$, **** $p < 0.001$ versus LPS; ### $p = 0.001$ versus RA/FBS(-) control). Statistical differences were calculated using Dunnett's multiple comparison test for one-way ANOVA.

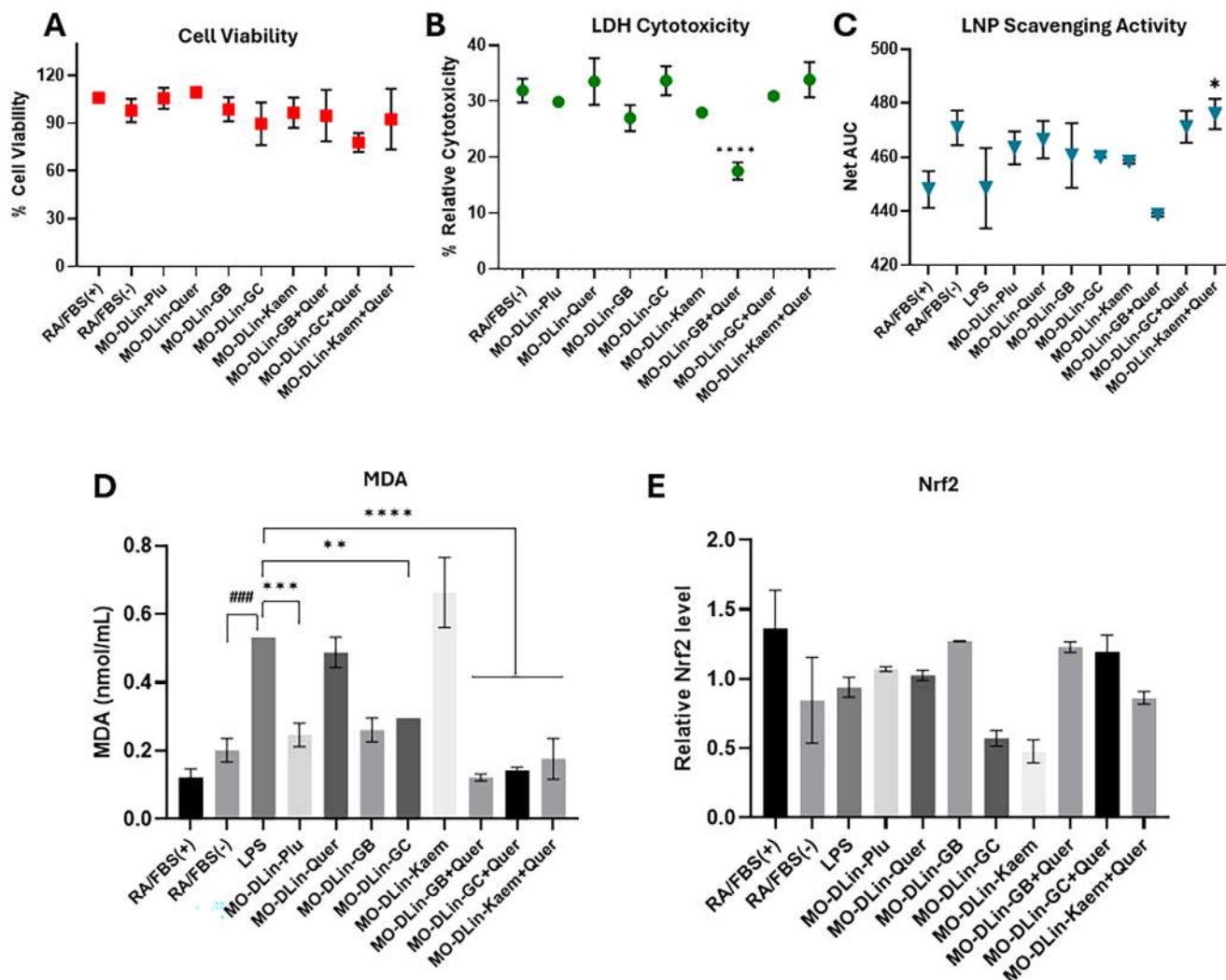


FIGURE 5 | In vitro evaluation of MO-DLin LNP formulations on cell viability, cytotoxicity, oxidative stress, and antioxidant response. (A, B) Cell viability and LDH cytotoxicity of treated cells are expressed as % relative to the control. Results are presented as mean \pm SD ($n = 3$, **** $p < 0.0001$ compared to LPS control). (C) Antioxidant capacity (ORAC) of LNP formulations evaluated by scavenging activity (Net AUC). Results are presented as mean \pm SD ($n = 2$, * $p < 0.05$ compared to LPS). (D) Lipid peroxidation was determined by MDA levels (nmol/mL). (E) Antioxidant response assessed by Nrf2 protein expression. Results are presented as mean \pm SD ($n = 3$, * $p < 0.05$, ** $p < 0.01$, *** $p < 0.001$, **** $p < 0.0001$, compared vs LPS stimulated group; ### $p < 0.001$ compared to RA/FBS(-) control). Statistical significance was calculated using one-way ANOVA followed by Dunnett's multiple comparisons test.

viability) compared to the control. The results indicate that the formulations were generally well tolerated at the tested concentrations (Figure 5A). This trend was also confirmed by the LDH cytotoxicity assay for the tested LNPs. As shown in Figure 5B, most treatment groups presented low to moderate cytotoxicity (>40% LDH). A significant reduction in LDH release was observed in the MO-DLin-GB+Quer group, suggesting a protective effect on cell membrane integrity.

Further studies by an ORAC assay were conducted to measure the antioxidant capacity of the studied LNPs to neutralize peroxy radicals (ROO \cdot), a product of oxidative stress (Figure 5C). SH-SY5Y cells were first subjected to LPS treatment, which led to a slight decrease in ORAC ($p = 0.0726$). The highest scavenging capacity was observed for MO-DLin LNPs co-encapsulating kamferol and quercetin. Although no significant difference was found between

the other LNP treatments, we observed an increasing trend in ORAC activity compared to the LPS control, which highlighted the potential of our MO-DLin LNPs as anti-ROS agents.

Lipid peroxidation was assessed by measuring malondialdehyde (MDA) levels in cell lysates following treatments (Figure 5D). LPS stimulation increased the MDA levels compared to the control group, confirming the induction of oxidative stress. This effect was counteracted by MO-DLin LNPs, particularly those containing quercetin combinations (MO-DLin-GB+Quer, MO-DLin-GC+Quer and MO-DLin-Kaem+Quer). The data in Figure 5D indicate that these LNP formulations effectively suppress lipid peroxidation and protect against LPS-induced oxidative stress.

The antioxidant response in relation to oxidative stress regulation was further assessed by Nrf2 protein expression (Figure 5E). The

Nrf2 levels were moderately increased in most treatment groups compared to the LPS group, with the MO-DLin-GC and MO-DLin-Kem groups showing the highest suppression and increased oxidative burden.

From a functional perspective, the coexistence of cubosome and hexosome populations at physiological pH may offer distinct advantages for cellular interaction. Cubosomes, with their bicontinuous cubic architecture and higher surface area, are known to facilitate rapid cellular adhesion and internalization via endocytic pathways, while hexosomes may preferentially fuse with cellular membranes owing to their intrinsic negative curvature. This topological heterogeneity may therefore result in a bimodal uptake profile. E.g., an initial rapid internalization process, driven by the cubosome fraction, followed by sustained membrane-mediated delivery from the hexosome population [43]. Moreover, the coexistence of phases at neutral pH implies that the system is poised near a phase boundary, enabling a rapid and cooperative structural reorganization upon encountering the acidic endosomal environment [44]. From a release kinetics perspective, the cubic phase, with its tortuous aqueous channel network, may provide a diffusion-controlled slow release of hydrophilic cargo (e.g., ginkgolides), whereas the hexosome domains, with their columnar aqueous channels, may permit more directional and rapid release upon acidification. This structural polydispersity, rather than being a limitation, may therefore represent a built-in mechanism for achieving both sustained extracellular stability and triggered intracellular release.

2.4 | Modulation of AKT/mTOR/GSK3 β /BDNF Signaling Pathway in Neuronal Survival and Anti-Apoptotic Response

AKT activity pathway, a critical regulator of neuronal survival, is modulated by phosphorylation at Thr308 or Ser473 residues, with Thr308 activation linked to dopamine receptor signaling and Ser473 regulated by NMDA receptor potentiation. We hypothesized that MO-DLin nanocarriers loaded with *Ginkgo biloba* actives may enhance phosphorylation of AKT at Ser473 (pAKTSer473). As shown in Figure 6A, treatment of SH-SY5Y cells with the DLin-LNP series significantly elevated pAKTSer473 expression compared to the LPS control (with the exception of the MO-DLin-Kaem+Quer formulation, which showed no significant change). Notably, the MO-DLin nanoformulations of GB/GC and GB/GC+Quer enhanced the expression of pAKTSer473 compared to the other nanoparticles. This selective activation suggested a mechanism-dependent response to LNP-encapsulated phytochemicals.

The observed pAKTSer473 profile closely parallels the LNP-induced changes in brain-derived neurotrophic factor (BDNF) expression (Figure 6B). The MO-DLin-Kaem+Quer formulation increased BDNF levels to nearly 4-fold, with significant elevations also noted for MO-DLin-GB+Quer and MO-DLin-GC+Quer, MO-DLin-Quer, MO-DLin-GB and MO-DLin-GC. This result indicated a potentially strong multi-target effect of AKT signaling and neurotrophic support.

Because AKT is a primary kinase inhibitor of glycogen synthase kinase-3 β (GSK-3 β) via phosphorylation at Ser9, we supposed

a corresponding modulation of pGSK-3 β Ser9. The performed analysis revealed no significant effect of the LNP treatments on pGSK-3 β Ser9 expression with the exception of the blank nanocarrier and MO-DLin-Kaem (Figure 6D). This suggested that GSK-3 β activity may not necessarily be a primary target for quercetin, GB, and GC under LPS-induced inflammatory conditions.

The role of mechanistic target of rapamycin (mTOR) in LNP-mediated neuroprotection was also explored. Figure 6C indicates that MO-DLin-Quer and MO-DLin-Kaem-LNPs significantly activated p-mTOR in LPS-stimulated SH-SY5Y cells, with MO-DLin-GC and MO-DLin-GC+Quer showing a moderate effect ($p = 0.0583$ and 0.1796 , respectively). Therefore, mTOR signaling may contribute to the neuroprotective effects of the specified LNP formulations.

2.5 | Effect of LNPs on Inflammatory Cytokines, Oxidative/Nitrosative Stress, and ER Stress/Apoptosis in LPS-Stimulated SH-SY5Y Cells

The proinflammatory response in SH-SY5Y cells is attributed to the activation of TLR4 by LPS, which triggers downstream inflammatory signaling pathways. The latter include NF- κ B and MAPK, leading to protein phosphorylation and nuclear translocation, and ultimately, the production of proinflammatory cytokines (e.g., IL-1 β , TNF- α , IL-6), ROS, and chemokines that perpetuate a neurotoxic microenvironment [12, 16]. To explore this further in LNP-mediated treatment, we examined inflammation-related pathways, including cytokine production (IL-1 β , NF- κ B), oxidative/nitrosative stress (nitrate), stress-activated signaling (JNK1/2), and ER stress/apoptosis (DDIT3/CHOP).

The effect of MO-DLin nanocarrier formulations on inflammatory and stress-related pathways in SH-SY5Y cells is shown in Figure 7. Nitrate is a stable end-product of nitric oxide (NO) metabolism, used as an indicator of cellular nitrosative stress. Even though the LPS concentration (1 μ g/mL) caused a significant increase in mitochondrial ROS (Figure 2C), the LPS effect was not statistically significant on nitrate activation (Figure 7A). It can be inferred that the formulations did not substantially affect nitrate levels except for MO-DLin-Kaem+Quer LNPs.

In contrast, the proinflammatory cytokine IL-1 β was significantly upregulated upon LPS induction. The process was significantly counteracted by the MO-DLin formulations, particularly by LNPs co-encapsulating two antioxidant compounds (Figure 7B).

Consistent with this effect, Nuclear factor-kappa B (NF- κ B) activity, a central regulator of inflammatory responses, was also significantly suppressed by antioxidant-loaded MO-DLin LNP formulations compared to LPS control (Figure 7C).

Stress-associated signaling pathways were assessed in addition to inflammatory regulation. JNK1/2 activity, which is typically increased under inflammatory and oxidative stress conditions, showed a modest but significant decrease in the MO-DLin-Quer, MO-DLin-GC+Quer and MO-DLin-Kaem+Quer groups (Figure 7D).

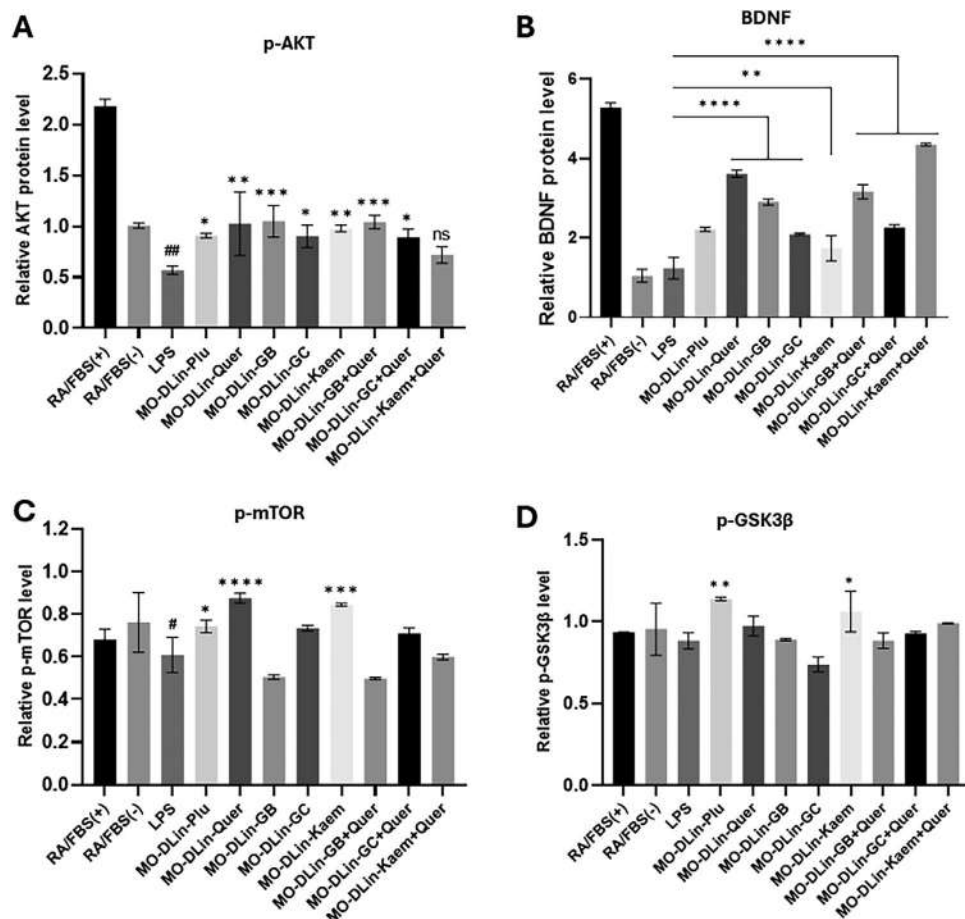


FIGURE 6 | Effects of MO-DLin-LNP nanoformulations on neuroprotective signaling pathways in LPS-stimulated SH-SY5Y cells. (A) Relative protein levels of phosphorylated AKT (p-AKT) and (B) Brain-Derived Neurotrophic Factor (BDNF). Results are presented as mean \pm SD ($n = 3$, * $p < 0.05$, ** $p < 0.01$, *** $p < 0.001$, **** $p < 0.0001$ compared to LPS; ## $p < 0.001$ vs RA/FBS(-) control). (C) Relative protein levels of phosphorylated mTOR (p-mTOR). Results are presented as mean \pm SD ($n = 3$, * $p < 0.05$, *** $p < 0.001$, **** $p < 0.0001$ compared to LPS; # $p < 0.05$ vs RA/FBS(-) group). (D) Relative protein levels of phosphorylated GSK3 β (p-GSK3 β). Data are presented as mean \pm SD ($n = 3$, * $p < 0.05$, ** $p < 0.01$ vs. LPS group). Statistical significance was calculated using one-way ANOVA by Dunnett's multiple comparisons test.

Additionally, the expression of DDIT3/CHOP, an established marker of endoplasmic reticulum stress, was slightly elevated in LPS-treated SH-SY5Y cells ($p = 0.0538$). Although MO-DLin formulations did not influence this pathway, a minimal reduction trend in DDIT3/CHOP levels was observed in phytochemical-loaded LNP formulations compared to the LPS group (Figure 7E).

2.6 | LNPs Attenuate MAPK/ERK and STAT3 Signaling while Preserving Tyrosine Hydroxylase Expression in LPS-Stimulated SH-SY5Y Cells

The MAPK/ERK pathway plays a critical role in modulating glial cell function and the inflammatory response in neurodegenerative diseases. This activation further engages inflammation-related pathways, including p-STAT3 and tyrosine hydroxylase. In our study, LPS stimulation decreased ERK phosphorylation (p-ERK) to levels comparable to those in serum-deprived SH-SY5Y cells (Figure 8A). Treatment with MO-DLin LNP series significantly upregulated p-ERK levels (Figure 8A). Similarly, p38 MAPK α , another stress-responsive kinase, was downregulated by several LNP formulations in comparison to the LPS-induced cells

(Figure 8B), suggesting a suppression of proinflammatory MAPK signaling. The inhibition of downstream inflammatory mediators (IL-1 β and NF- κ B) was also observed (Figure 7).

Phosphorylated STAT3 (p-STAT3), a transcription factor linked to cytokine signaling and neuroinflammation, was slightly decreased upon LPS induction but attenuated following treatment with MO-DLin-based formulations (MO-DLin-Plu, MO-DLin-Quer, MO-DLin-GB, MO-DLin-GB-Quer, and MO-DLin-GB-Quer (Figure 8C). In contrast, tyrosine hydroxylase (TH), a critical enzyme in dopamine biosynthesis, did not show significant alterations across groups (Figure 8D), which establishes that dopaminergic enzyme regulation is unaffected under these conditions.

3 | Discussion

The results of the present study demonstrate the therapeutic potential of biomimetic nanomedicines engineered with liquid-crystalline material properties, pH-responsiveness, and key activities yielding superior biological outcomes. A central question is

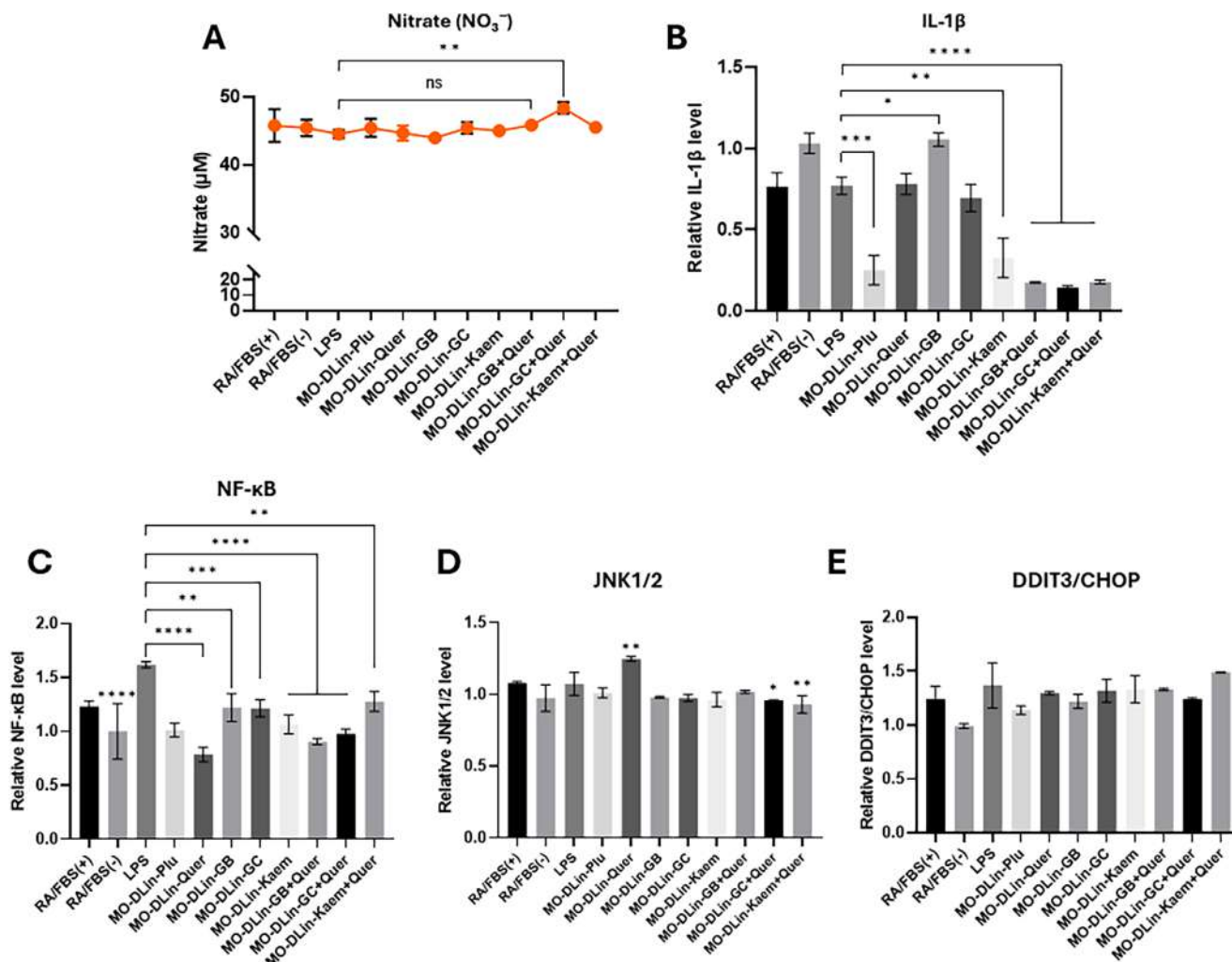


FIGURE 7 | Effects of MO-DLin LNP formulations on inflammatory and stress-related pathways in LPS-stimulated SH-SY5Y cells. (A) Nitrate (NO_3^-) levels measured by a fluorometric assay. (B) Relative interleukin-1 β (IL-1 β) levels following treatment with the MO-DLin LNP series. Data are presented as mean \pm SD ($n = 3$, * $p < 0.05$, ** $p < 0.01$, *** $p < 0.001$, **** $p < 0.0001$ compared to LPS control). (C) Relative NF- κ B activity. Data are presented as mean \pm SD ($n = 3$, ** $p < 0.01$, *** $p < 0.001$, **** $p < 0.0001$ compared to LPS control). (D) Relative expression of JNK1/2, and (E) Relative DDIT3/CHOP expression. Data are presented as mean \pm SD ($n = 3$, * $p < 0.05$, ** $p < 0.01$ compared to LPS control). Statistical significance was calculated using one-way ANOVA by Dunnett's multiple comparisons test.

how the observed pH-dependent cubosome-to-hexosome structural transition may facilitate enhanced intracellular delivery. We hypothesize that under the acidic conditions of early and late endosomes (pH \approx 5.0–6.5), protonation of DLin's tertiary amine headgroup increases the proportion of the inverted hexagonal (H_{II}) phase domains within the LNP interior. The H_{II} phase topology, characterized by tightly curved lipid cylinders surrounding aqueous channels, is thermodynamically conducive to fusion with the endosomal membrane. Specifically, the negative curvature of the H_{II} phase can generate non-bilayer lipid intermediates at the LNP-endosomal membrane interface, destabilizing the endosomal bilayer and promoting cargo translocation into the cytoplasm. This mechanism is analogous to the established endosomal escape pathway described for DLin in mRNA-LNP delivery, where ion pairing between the protonated ionizable lipid and anionic endosomal phospholipids drives the formation of membrane-disruptive hexagonal phases [25, 28]. Thus, the structural responsiveness characterized by SAXS is not merely a physico-chemical phenomenon but is proposed to

be a functionally enabling feature that enhances the cytoplasmic bioavailability of the encapsulated phytochemicals beyond what passive diffusion or conventional liposomal carriers would achieve.

In addition to the internal nanostructure, the hydrodynamic size and distribution of the LNPs are important physicochemical parameters influencing biological performance. Dynamic light scattering (DLS) analysis revealed that drug-loaded formulations exhibited increased mean hydrodynamic diameters and moderate polydispersity (PDI \approx 0.2–0.3) (Table S2). This increase can be attributed not only to drug incorporation but also to the anisotropic nature of the hexosome particles. These particles consist of elongated cylindrical domains arranged in an inverted hexagonal lattice (as evidenced by the SAXS results in Figure 2), rather than in ideal spherical geometries. It is essential to emphasize that the preservation of well-defined internal hexagonal order requires a sufficiently large structural domain size. A significant reduction in the dispersed particle size would decrease the

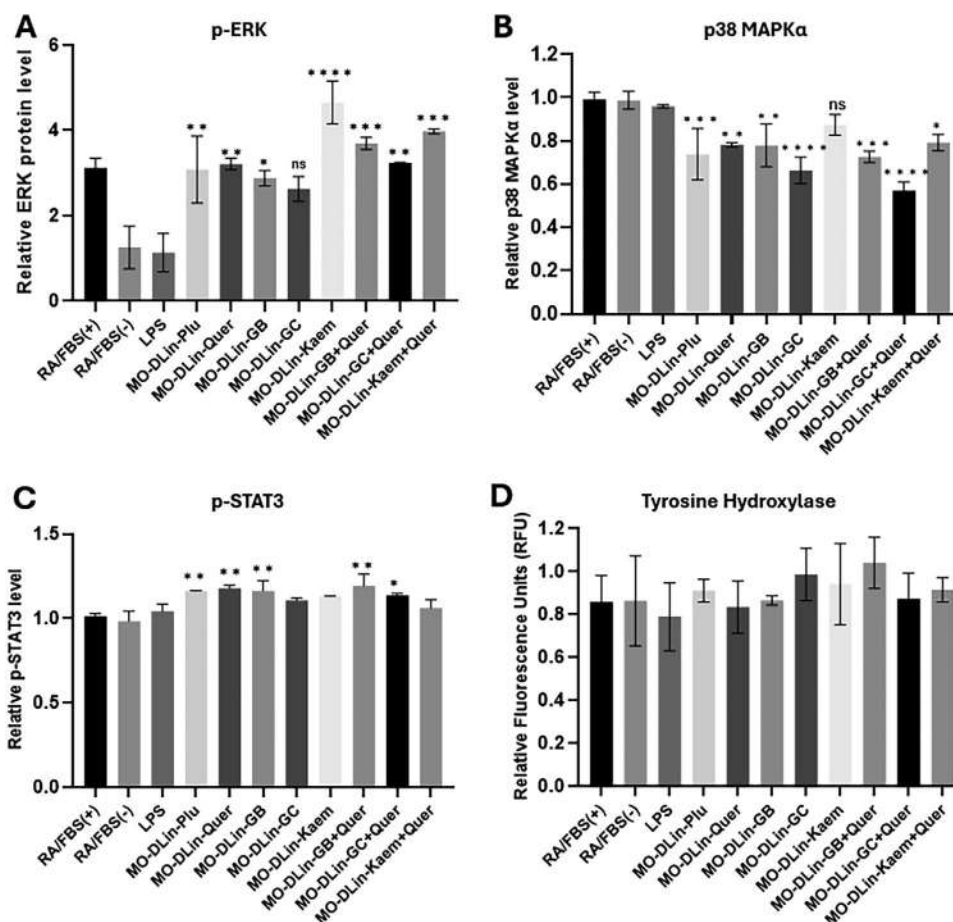


FIGURE 8 | MO-DLin nanoparticles regulate MAPK/ERK, STAT3, and tyrosine hydroxylase signaling in LPS-stimulated SH-SY5Y cells. (A) Phosphorylation of ERK (p-ERK) and (B) p38 MAPK α levels in LPS-treated SH-SY5Y cells. (C) LPS-induced phosphorylation of STAT3 (p-STAT3) is significantly attenuated following treatment with MO-DLin-based nanoformulations. (D) Tyrosine hydroxylase (TH) expression after treatment with MO-DLin LNPs. Data are presented as mean \pm SD, with statistical significance indicated by * p < 0.05, ** p < 0.01, *** p < 0.001, **** p < 0.0001 compared to the LPS group. Statistical significances were calculated using Dunnett's multiple comparison test for one-way ANOVA.

number of repeating lattice units, leading to diminished or poorly resolved Bragg peaks. Therefore, the observed hydrodynamic size range is consistent with the presence of structurally ordered hexosomes [45, 46].

From a biological perspective, while smaller and more monodisperse nanoparticles are often considered optimal for intracellular delivery, particles in the 200–500 nm range can still be internalized via alternative endocytic pathways such as caveolae-mediated uptake and macropinocytosis [47, 48]. This suggests that the moderate size heterogeneity observed here may contribute to variability in uptake efficiency and batch-to-batch responses. Nevertheless, the retained biological activity indicates that the formulations remain functionally competent, while further optimization of size distribution could enhance reproducibility.

The ionizable MO-DLin lipid-based nanoparticles, incorporating multi-target antioxidants from *Ginkgo biloba* (quercetin, ginkgolide B, ginkgolide C, and kaempferol) in the liquid crystalline matrix, effectively mitigated LPS-induced oxidative stress, neuroinflammation, and apoptotic signaling in differentiated SH-SY5Y cells, a representative in vitro model of neurodegeneration.

The novelty of our work lies at the intersection of materials science and nanotechnology in the context of modulation of neuroinflammatory and oxidative stress pathways. The reported here innovative features include: (i) ionizable pH-responsive material design comprised of lyotropic liquid crystalline nanoparticles incorporating the clinically validated ionizable lipid DLin, which favors structural dynamics and higher intracellular drug concentration; (ii) multi-functionalization for neuronanomedicine with a unique integrated design that simultaneously deploys antioxidant, anti-inflammatory, and neurotrophic actions; and (iii) advanced nanoscale architecture of a potent delivery system tailored for the challenges of treating neurological disorders.

Figure 9 summarizes the in vitro therapeutic potential of the antioxidant-loaded MO-DLin LNPs evaluated by targeting the interconnected axes of oxidative stress, inflammation, and mitochondrial dysfunction in LPS-challenged human cells.

Our study focused on three interlinked pathways that underlie neuronal survival and degeneration. First, the ROS/mitochondrial stress and inflammation, which induce cytokine release and neuronal death. We demonstrated that LPS stimulation significantly elevated mitochondrial superoxide

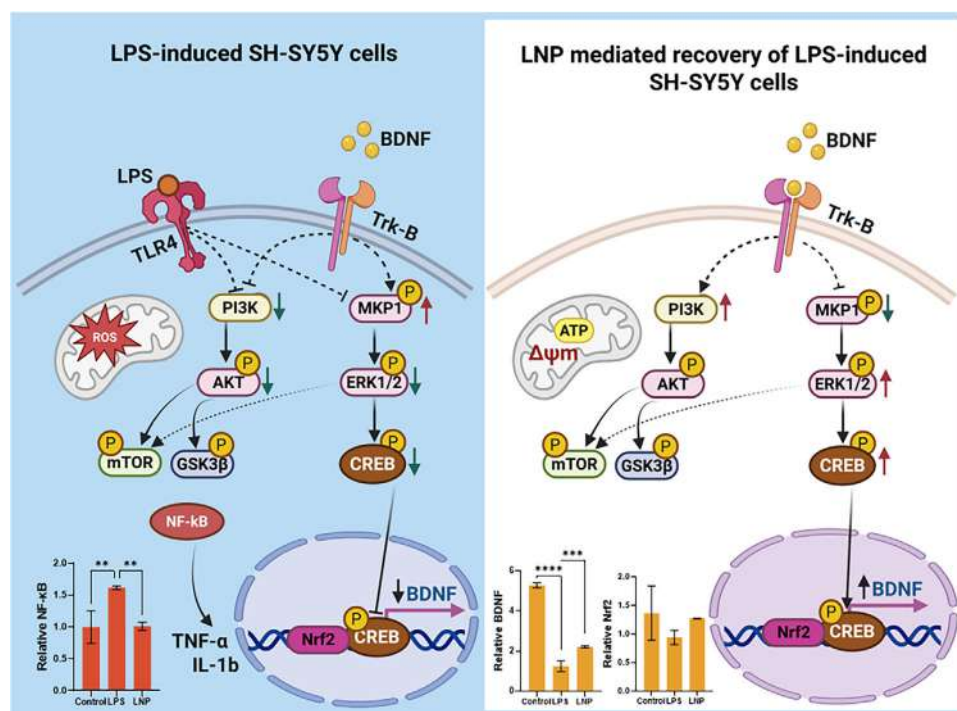


FIGURE 9 | Schematic representation of signaling alterations in LPS-challenged differentiated SH-SY5Y cells (left) followed by recovery through LNP treatment (right). LPS stimulation activates TLR4, leading to increased ROS, NF-κB signaling, and induction of proinflammatory cytokines (TNF-α, IL-1β), with a simultaneous downregulation of PI3K/AKT/mTOR and BDNF/TrkB pathways, suppression of Nrf2, and enhanced GSK3β activity, favouring apoptosis and inflammation. In a recovery approach, MO-DLin LNP-mediated treatment restores BDNF/TrkB-driven PI3K/AKT/mTOR and ERK/CREB signaling, enhances Nrf2 activation, improves mitochondrial function (ATP, Δψm), and promotes neuronal survival and plasticity. Bar graphs indicate relative expression changes of NF-κB, BDNF, and Nrf2 in control, LPS, and LNP-treated cells (created with BioRender).

levels in SH-SY5Y cells, as detected by MitoSOX Red, mimicking the oxidative burden observed in PD and AD models. Notably, MO-DLin-based LNPs loaded with quercetin, GB, or co-encapsulation of quercetin/GC/kaem effectively scavenged free radicals, reducing MitoSOX-positive cells and MDA levels. The antioxidant compounds employed in this study have demonstrated antioxidative and neuroprotective properties against CNS diseases [49]. These compounds contribute to enhanced neuronal survival through multiple mechanisms, including stabilization of mitochondrial membrane potential, activation of Nrf2-mediated antioxidant defences, attenuation of TLR4/NF-κB-driven neuroinflammation, and regulation of intracellular Ca^{2+} influx and homeostasis. In addition, they have been reported to decrease lipid peroxidation, promote mitochondrial biogenesis via the AMPK/PGC-1α-TFAM signaling to improve cellular energy metabolism, and act as anti-inflammatory antioxidants by upregulating heme oxygenase-1 (HO-1) through the ROS-dependent Nrf2-ARE cascade. The dual-payload approach in the studied LNPs, such as combining Quer+GC/ Quer+Kaemferol in lipid nanocarriers, amplified the antioxidant beneficial properties, yielding superior ORAC activity.

Secondly, we exploited the antioxidant defense mechanisms, primarily the Nrf2/ARE pathway, which regulates the expression of cytoprotective enzymes such as HO-1, NQO1, and SOD to restore redox balance [50]. This process liberates phosphorylated Nrf2 from the Keap1 complex, enabling its translocation into the nucleus, where it binds to ARE promoter regions and induces

transcription of phase II antioxidant enzymes, including HO-1 [46–56]. While excessive oxidative stress results in elevated intracellular ROS levels, which damage DNA, proteins, and lipids, a moderate increase in ROS is essential for maintaining cellular homeostasis and activating key signaling pathways.

In our study, we observed that phospho-Nrf2 was slightly downregulated in the LPS-induced models, a response which was subsequently counteracted by most of the MO-DLin-based formulations. Interestingly, treatment with MO-DLin-Kaem and MO-DLin-GC led to suppression of Nrf2 expression. However, when co-encapsulated with quercetin, Nrf2 levels were slightly restored. This finding suggests potential multi-modal interactions between different polyphenols within the LNP system, where quercetin may counteract the suppressive effects of other compounds and enhance Nrf2-mediated antioxidant signaling.

Finally, we examined the LNP-mediated modulation of the survival and neurotrophic signaling cascades, i.e. PI3K/AKT/mTOR/GSK3β and MAPK/ERK/CREB, as well as BDNF expression. Particularly, the BDNF pathway is linked with the activation of multiple intracellular signaling cascades, most notably the ERK pathway and the PI3K/AKT/mTOR pathway, which together regulate neuronal survival, growth, and synaptic plasticity (Figure 9). Beyond antioxidant effects, the studied LNPs modulated critical signaling pathways implicated in neuronal survival and inflammation. LPS-induced activation of the MAPK/ERK pathway, a key mediator of glial-driven neuroinflammation, was attenuated by simultaneously

downregulating p38 MAPK α and upregulating p-ERK in treated cells, consistent with reports that ERK/MAPK signaling exacerbates cytokine production and oxidative damage in microglial activation models [39].

Moreover, p-STAT3, a downstream effector linked to IL-1 β and NF- κ B-driven inflammation, was significantly enhanced by specific MO-DLin-based formulations, while this effect did not reflect in tyrosine hydroxylase (TH) expression, even though an increasing tendency was observed. Furthermore, the enhanced p-AKT (Ser473) and BDNF levels induced the activation of pro-survival AKT/mTOR signaling, which inhibits GSK-3 β and promotes synaptic plasticity mechanisms. Although p-GSK-3 β (Ser9) showed minimal changes for specific nanoparticles, this may reflect LNP-specific regulation.

An important finding is that inflammatory mediators, including IL-1 β and NF- κ B, were suppressed through inhibition of TLR4-mediated inflammatory responses, with minimal impact on ER stress marker DDIT3/CHOP. In contrast, JNK1/2 signaling was selectively modulated by specific formulations, namely MO-DLin-Quer, MO-DLin-GC+Quer, and MO-DLin-Kaem+Quer.

In perspective, the encapsulation of bioactives within MO-DLin-Plu LNPs may effectively address key challenges in brain delivery, including bioavailability and blood-brain barrier (BBB) targeting. LNPs show promise in nose-to-brain delivery and targeted neuronal uptake, as demonstrated in studies where functionalized LNPs co-encapsulating antioxidants like curcumin or quercetin enhance CNS accumulation and neuroprotective efficacy [42–44, 49–53]. Ultimately, our work advances the concept of mitochondria-targeted nanomedicines, paving the way for innovative therapeutic strategies in neurodegenerative disorders.

4 | Conclusion

In conclusion, we successfully designed, formulated, and characterized a class of ionizable pH-responsive lyotropic liquid crystalline nanocarriers as an advanced materials platform for neuroprotective and anti-inflammatory applications. The incorporation of the clinically validated, ionizable lipid DLin confers pH-responsiveness of the LNPs to the acidic pathological microenvironment, a critical feature for enabling efficient intracellular delivery of therapeutic agents under neurodegenerative conditions. Our comprehensive in vitro studies demonstrated that the self-assembled MO-DLin-Plu nanocarriers, loaded with a combination of phytochemical actives from *Ginkgo biloba* extract, effectively mitigate oxidative stress and activate pro-survival signaling in a cellular model of neurodegeneration.

The reported findings highlight the significant potential of rationally designed multifunctional LNP-nanoantioxidants to address the complex pathology of neurodegenerative diseases. Our results demonstrated that the MO-DLin-based nano-antioxidants not only inhibited ROS in vitro (reduced MitoSOX signal and MDA) but also upregulated the Nrf2 axis to maintain redox homeostasis while suppressing TLR4/NF- κ B and IL-1 β -mediated inflammation. Moreover, the formulations enhanced pro-survival and neurotrophic signaling (p-AKT/p-mTOR and BDNF), preserved mitochondrial function ($\Delta\Psi_m$) in differentiated SH-SY5Y cells,

and selectively modulated MAPK/ERK and STAT3 activity pathways, which are essential for maintaining neuronal survival and regulating inflammatory balance.

The MO-DLin-based LNPs achieved targeted intracellular delivery of quercetin, ginkgolides B/C, and kaempferol nano-antioxidants. The co-encapsulation significantly inhibited IL-1 β expression in comparison to single-payload delivery. The unique structural properties and the dynamic architectures of the ionizable MO-DLin-based nanocarriers represent a substantial advancement over conventional lipid systems. It offers a versatile strategy for the development of next-generation neurotherapeutics with a promise to overcome translational barriers in antioxidant-based neuroprotective therapy.

5 | Experimental Section

5.1 | Materials for Lipid Nanoparticle Preparation

The ionizable cationic lipid DLin-MC3-DMA (Dilinoleyl-methyl-4-dimethylaminobutyrate) (MW 642.1; apparent pKa = 6.45) was purchased from Broadpharm. Monoolein (MO, C18:1c9, powder, $\geq 99\%$), Pluronic F127 (PLU-F127), quercetin (Quer), retinoic acid (RA), 2,6-di-tertbutyl-4-methylphenol (BHT), and Lipopolysaccharides (LPS) were purchased from Sigma-Aldrich. The active compounds Ginkgolide B (GB), Ginkgolide C (GC), and kaempferol (Kaem) were purchased from MedChemExpress, while FCCP and Trolox were purchased from Cayman Chemical. Water of MilliQ quality (Millipore Corp., Molsheim, France) was used for the preparation of a phosphate buffer solution (NaH₂PO₄/Na₂HPO₄, 1×10^{-2} M, pH 7, p.a. grade, Merck).

For LNP preparation, mixed thin lipid films were hydrated and dispersed at room temperature in a 1×10^{-2} M phosphate buffer (pH 7.4) containing BHT. The phosphate buffer with BHT was purged with nitrogen gas to eliminate dissolved oxygen and then filtered through a 0.2 μ m sterile filter (Millipore Corp.).

5.2 | Preparation of Ionizable Lipid Nanoparticles

Liquid crystalline nanoparticles were fabricated by hydrating lyophilized thin lipid films and then subjecting the dispersion to physical agitation in an excess aqueous phase. The lipids MO and DLin-MC3-DMA, the amphiphilic stabilizer Pluronic F127 (PLU-F127), and the antioxidants GB, GC, Kaem, and Quer, were weighed, dissolved in chloroform, and mixed at desired proportions. The solvent was evaporated under a stream of nitrogen gas for 30 min at room temperature in a fume hood to form a thin lipid film. The obtained films were further lyophilized overnight under cooling to remove residual solvent. The dried films were then hydrated and dispersed at room temperature in a 1×10^{-2} M phosphate buffer (pH 7.4) containing BHT as an antioxidant. The buffer was pre-purged with nitrogen gas to eliminate dissolved oxygen and subsequently passed through a 0.2 μ m sterile filter (Millipore Corp.). The resulting mixtures were subjected to physical agitation and sonication in an ultrasonic ice bath (42 kHz, 15 min) to promote fragmentation and self-assembly of the nanoparticles. This procedure facilitated the formation of ionizable nanoparticle LNPs [57]. The mean hydrodynamic

diameters (d_h) and polydispersity indices of LCNPs obtained by spontaneous self-assembly and dispersion of hydrated lipid mixtures of MO and DLin, stabilized by PLU-F127, were also determined using dynamic light scattering (DLS) (Table S2).

5.3 | Synchrotron Small-Angle X-Ray Scattering (SAXS) Characterization

SAXS experiments were carried out at the ID02 beamline of the European Synchrotron Radiation Facility (ESRF) (Grenoble, France). Measurements were performed using an incident X-ray beam with an energy of 12.23 eV ($\lambda = 1.013 \text{ \AA}$), a photon flux of 1.18×10^{12} photons per second, and a sample-to-detector distance of 2 m [58–60]. Under these conditions, the accessible scattering vector range ($q = 4\pi\sin\theta/\lambda$, with θ being the scattering angle) extended from about 0.003 to 0.37 \AA^{-1} . Samples were introduced into a flow-through capillary cell with a diameter $\phi = 2 \text{ mm}$, equipped with Peltier temperature control. Each exposure lasted 0.1 s, and scattering data were recorded with an Eiger $2 \times 4 \text{ M}$ pixel array detector (Dectris). The resulting two-dimensional scattering patterns were normalized to an absolute intensity scale, and azimuthal averaging yielded one-dimensional intensity profiles [61]. All measurements were conducted at 22°C . Background scattering from a phosphate buffer solution (pH 7.4 or pH 5.0) was subtracted from each dataset. Data reduction and analysis were performed with the ATSAS 3.3.0 package, using the PRIMUS interface.

Lattice parameters of liquid-crystalline lipid phases were determined from the positions of Bragg reflections in the diffraction patterns. For cubic phases, the lattice constant (a_Q) was calculated using the relationship $a_Q = d(h^2 + k^2 + l^2)^{1/2}$, where the repeat spacing (d) is obtained from Bragg's law ($d = 2\pi/q$). This can also be expressed as $1/d^2 = (h^2 + k^2 + l^2)/a^2$. The Miller indices (hkl) were used to assign the observed Bragg peaks.

For lamellar arrangements, the reflections occur at integer multiples of the fundamental spacing ($a/d = 1, 2, 3, \dots$).

For a cubic liquid crystalline phase of the primitive type ($Im3m$ space group), the squared ratios follow the sequence $(a/d)^2 = 2, 4, 6, 8, 10, 12, 14, 16, 18, 20, 22$.

For hexagonal phases, the lattice parameter (a_H) was determined from $a = d [2/\sqrt{3} (h^2 + k^2 - hk)]^{1/2}$ [62, 63].

5.4 | Cell Culture Methods

The human SH-SY5Y neuroblastoma cells, available from previous research in the lab, were differentiated and used as an in vitro neuronal model. Cells were cultured in high-glucose Dulbecco's Modified Eagle's Medium (DMEM) supplemented with 10% fetal bovine serum (FBS) and 1% penicillin–streptomycin (Pen/Strep), and maintained at 37°C in a humidified atmosphere of 5% CO_2 . Calcium and magnesium-free phosphate-buffered saline (PBS), FBS, Pen/Strep, trypsin, dimethyl sulfoxide (DMSO), and 3-(4,5-dimethylthiazol-2-yl)-2,5-diphenyltetrazolium bromide (MTT) were obtained from Sigma-Aldrich. Neuronal differentiation was induced with

10 μM retinoic acid for 5 days. SH-SY5Y cells were treated with 1 $\mu\text{g/mL}$ LPS followed by LNP exposure for 24 h for the various bioassays. Wells or culture flasks were assigned to treatment groups according to the experimental design, which included control (controls, LPS-stimulated, and LPS + LNP-treated).

5.5 | Cytotoxicity and Cell Viability Assays

The human SH-SY5Y neuroblastoma cells were plated in 96-well plates at 1×10^4 cells per well and allowed to attach overnight at 37°C in 5% CO_2 . The following day, the medium was replaced with complete DMEM containing 10 μM retinoic acid (RA), and cells were differentiated for 5 days with routine microscopic checks. Differentiated cultures were then treated for 24 h with nanoparticle formulations. RA-differentiated cells subjected to 24 h serum-free medium (RA/FBS(–)) served as reference control.

For LDH release, 90 μL of cell-free supernatant from each well was transferred to a fresh 96-well plate, 10 μL of LDH Cytotoxicity Reagent (CytoSelect kit, CBA-241) was added, and plates were incubated for 30 min at 37°C before reading absorbance at 450 nm. For MTT viability measurements, the adherent cells remaining in the original plate received 20 μL of freshly prepared MTT solution (5 mg/mL in PBS) and were incubated for 1 h at 37°C ; the medium was then removed, and the formazan crystals were dissolved in DMSO. The absorbance was recorded at 570 nm. Viability was calculated as a percentage relative to the RA/FBS(–) control. To exclude potential optical interference, positive (10% Triton X-100) and negative (untreated) controls were used to define maximal and baseline LDH release, respectively.

5.6 | Quantification of Phosphorylated AKT and ERK by ELISA

The levels of phosphorylated ERK1/2 and AKT in lysates from nanoparticle-treated SH-SY5Y cells were measured with commercial ELISAs (Phospho-ERK1/2 DuoSet IC, Cat. DYC1018B-5; Phospho-AKT Pan-Specific DuoSet IC, Cat. DYC887B-5; Bio-Techne/R&D/R&D Systems, UK). The assays detect phosphorylation at ERK1/2 Thr202/Tyr204 and Thr185/Tyr187, and at AKT Ser473. Cell lysis was performed using the buffer supplied in the DuoSet IC ancillary kit (Cat. DY008). Monoclonal antibody-coated 96-well plates were incubated with standards or samples for 2 h, followed by enzyme-conjugated detection antibodies for 1 h at room temperature. Blank wells without cell lysate or LNPs and RA/FBS(–) cells without LNP treatment were included in parallel as controls. After three wash steps, substrate was added, and the reaction was stopped before reading absorbance at 450 nm. Signal intensity reflected the amount of phosphorylated AKT and ERK.

5.7 | Human BDNF ELISA

Human free BDNF was quantified in SH-SY5Y cells after 24 h nanoparticle exposure using the Human Free BDNF ELISA (Cat. DBD00; R&D Systems, Bio-Techne, UK). Pre-coated plates received 50 μL of standards, controls (blank and untreated cells

RA/FBS(–)), or samples plus 100 μ L assay diluent followed by a 2 h incubation period. The wells were then treated with 100 μ L of HRP-conjugated anti-BDNF antibody for 1 h, washed three times and the color was developed with 200 μ L substrate in the dark for 30 min, and stopped with 50 μ L stop solution. The absorbance at 450 nm was recorded within 30 min.

5.8 | Phospho-p38 MAPK α and Phospho-STAT3 Detection

Phosphorylated p38 MAPK α and STAT3 (Tyr705) were measured using sandwich ELISAs (Abcam ab221013 and ab126459), following the manufacturers' protocols. SH-SY5Y cells were lysed in kit-supplied buffers containing protease and phosphatase inhibitors, and protein concentration was determined by BCA. Equal volumes of sample lysate and control (100 μ L) were added to the capture antibody-coated wells and incubated for 2.5 h at room temperature. The controls included untreated RA/FBS(–) cells as baseline control and blank wells without LNPs or cells. After washing, phospho-specific detection antibodies (p-p38 Thr180/Tyr182 or p-STAT3 Tyr705) were applied, followed by HRP-linked secondary antibodies for 1 h. The reactions were developed with TMB and read at 450 nm.

5.9 | Mitochondrial Superoxide Detection

Mitochondrial superoxide was assessed using the Mitochondrial Superoxide Dye (STEMCELL Technologies, Cat. 100–0991). Cells were seeded at 3×10^5 per well, treated with LNPs for 24 h, then stained according to the manufacturer's instructions. Fluorescence was measured by microscopy with a FLUOstar OPTIMA plate reader (excitation/emission 510/580 nm). The fluorescence intensity corresponded to mitochondrial superoxide levels under each treatment condition.

5.10 | Lipid Peroxidation (MDA assay)

Malondialdehyde (MDA) was quantified using the Lipid Peroxidation Assay Kit (Sigma-Aldrich, MAK085). For sample preparation, 5×10^6 cells were homogenized on ice in 300 μ L MDA Lysis Buffer containing 3 μ L of 100 \times butylated hydroxytoluene to prevent further oxidation. The samples were centrifuged at $13\,000 \times g$ for 10 min at 4°C, and the supernatant was stored for further experiments. For the assay, 200 μ L of each sample supernatant, control or standard was mixed with 600 μ L freshly prepared TBA solution, vortexed, and incubated at 95°C for 60 min to form MDA-TBA adducts. The samples were cooled on ice, centrifuged to remove particulates, and the absorbance was recorded at 540 nm on a microplate reader.

5.11 | Total NF- κ B p65 and JNK1/2

These assays were performed using commercial ELISA kits (Abcam SimpleStep; NF- κ B p65 Total, ab176648; JNK1/2 Total, ab176646). Following treatments, SH-SY5Y cultures were rinsed twice with ice-cold PBS and lysed on ice in 1 \times Cell Extraction Buffer PTR supplemented with the kit Extraction Enhancer and

phosphatase inhibitors (protease inhibitors added as needed). Lysates were clarified by centrifugation ($14\,000 \times g$, 10 min, 4°C), and protein concentration was determined by BCA. Both assays were run according to the manufacturer's protocols. Pre-coated 96-well strip plates were loaded with 50 μ L of sample or kit control lysate, followed immediately by 50 μ L of freshly mixed Antibody Cocktail (capture and detector antibodies, 1:1 dilution). The plates were incubated for 1 h, followed by a wash step. The color development was obtained with the addition of 100 μ L TMB substrate for 15 min in the dark and the reactions were stopped with 100 μ L stop solution. The absorbance was read at 450 nm on a microplate reader. Each test included duplicate blanks (buffer only) and the kit-supplied positive control lysate (NF- κ B p65 and JNK1/2 control).

5.12 | DDIT3/CHOP Cell-Based ELISA

The relative expression of DDIT3/CHOP was analyzed by Abnova KA5679 cell-based ELISA. SH-SY5Y cells were seeded (3×10^5) in sterile, clear-bottom 96-well culture plates and allowed to reach 70% confluence. After removing the medium, wells were rinsed, and the cells were fixed at room temperature in 4% formaldehyde for 20 min. The fixative was removed and the wells were washed three times with 1 \times Wash Buffer, then incubated with quenching buffer for 20 min to suppress endogenous peroxidase activity. Following additional washes, nonspecific binding was blocked with blocking buffer for 1 h at room temperature. The primary antibodies (anti-GADD153/DDIT3 and anti-GAPDH) were then incubated overnight at 4°C. HRP-conjugated secondary antibodies were added for 1.5 h at room temperature with gentle shaking (anti-rabbit HRP for DDIT3 and anti-mouse HRP for GAPDH). The colour was developed with Ready-to-use TMB substrate for 30 min in the dark, and absorbance was read at 450 nm on a microplate reader.

5.13 | Human IL-1 β ELISA

Cell-culture supernatants from treated SH-SY5Y cells were collected and briefly centrifuged to remove debris. Human IL-1 β was quantified using the Human IL-1 beta ELISA Kit (Sigma-Aldrich/Merck, RAB0273) according to the manufacturer's instructions. Briefly, 100 μ L of undiluted samples and control were added to the anti-IL-1 β -coated plate and incubated for 2.5 h at room temperature with gentle shaking. Wells were washed, followed by incubation of 100 μ L of the biotinylated anti-IL-1 β detection antibody. Then, 100 μ L HRP-streptavidin was added for 45 min, followed by the addition of 100 μ L TMB One-Step Substrate. The reaction was stopped with 50 μ L Stop Solution, and the absorbance was read at 450 nm.

5.14 | Phospho/Total GSK3 β , and mTOR ELISA

Phospho/Total GSK3 β , and mTOR ELISA was quantified using Abcam Phospho-AKT/ GSK3 β / mTOR ELISA (ab279732). Pre-coated plates were incubated with 100 μ L of diluted samples, and the kit NIH/3T3 positive-control dilution series was added to designated wells and incubated at room temperature with gentle shaking. Following a wash step, the plate was incubated with

the target-specific rabbit primary antibodies provided for each readout: phospho-GSK3 β (Ser9), total GSK3 β , phospho-mTOR (Ser2448), and total mTOR. After each primary incubation and wash, HRP-conjugated anti-rabbit IgG was loaded onto the plates. Following the final wash, the color was developed with TMB One-Step Substrate at room temperature in the dark, and the absorbance was read at 450 nm on a microplate reader.

5.15 | Assessment of Total Protein Concentration

Total protein levels in cell lysates were quantified using the Bradford assay in a 96-well microplate format. A standard curve was generated using bovine serum albumin (BSA) prepared at 2 mg/mL in PBS and serially diluted to produce seven concentration standards. For each determination, 20 μ L of either the BSA standard or the cell lysate sample was combined with 180 μ L of Bradford reagent (Sigma, Cat. #B6916-500 mL). Absorbance was recorded at 595 nm with a microplate reader, and background absorbance from a blank well was subtracted. The concentrations of phosphorylated AKT, ERK1/2, BDNF, NF κ B, IL-1 β , JNK, and GSK3 β /mTOR were normalized to the total protein content of their corresponding lysates.

5.16 | Statistical Analysis

Statistical analyses were performed using GraphPad Prism version 9.5.1, and results are expressed as mean \pm SD. For two-group comparisons, an independent Student's t-test was applied, whereas one-way and two-way ANOVA were used for multiple-group analyses. A p -value < 0.05 was considered statistically significant. In addition, the sigmoidal four-parameter logistic (4PL) model was employed to evaluate the relationship between cellular responses and protein expression levels.

Acknowledgements

Thelma Akanchise acknowledges the support of a PhD fellowship from Campus France. Angelina Angelova acknowledges the PHC Ștefanik project 53619ZF. The authors thank ESRF for granting beam time for SAXS experiments at the ID02 beamline (project SC-5591) and acknowledge insightful discussions with Dr. Theyencheri Narayanan and scientific and technical support by Dr. Gouranga Manna. T.A. is grateful to Mélanie Hery (Cell Culture Platform) for cell culture advice. Figures 1 and 9 were created with BioRender.com (accessed August 10, 2025).

Open access publication funding provided by COUPERIN CY26.

Conflicts of Interest

The authors declare no conflict of interest.

Data Availability Statement

The data that support the findings of this study are available from the corresponding author upon reasonable request. All data, materials, and methods are included in the article.

References

1. R. AlRuwalli, H. M. Al-kuraishy, A. I. Al-Gareeb, et al., "Targeting of the PI3 K/AKT/GSK3 β Pathway in Parkinson's Disease: a Therapeutic

Blueprint," *Molecular Neurobiology* 62 (2025): 15108–15131, <https://doi.org/10.1007/s12035-025-05113-y>.

2. X. Du, X. Wang, and M. Geng, "Alzheimer's Disease Hypothesis and Related Therapies," *Translational Neurodegeneration* 7, no. 1 (2018): 2, <https://doi.org/10.1186/s40035-018-0107-y>.

3. A. R. Rao, S. M. Hidayathullah, K. Hegde, and A. P. Parkinsonism, "Parkinsonism: an Emerging Post COVID Sequelae," *IDCases* 27 (2022): e01388, <https://doi.org/10.1016/j.idcr.2022.e01388>.

4. R. Lee Mosley, E. J. Benner, I. Kadiu, et al., "Neuroinflammation, Oxidative Stress, and the Pathogenesis of Parkinson's Disease," *Clinical Neuroscience Research* 6, no. 5 (2006): 261–281, <https://doi.org/10.1016/j.cnr.2006.09.006>.

5. B. S. Daraban, A. S. Popa, and M. S. Stan, "Latest Perspectives on Alzheimer's Disease Treatment: the Role of Blood-Brain Barrier and Antioxidant-Based Drug Delivery Systems," *Molecules (Basel, Switzerland)* 29, no. 17 (2024): 4056, <https://doi.org/10.3390/molecules29174056>.

6. C.-Y. Huang, J.-Y. Chen, C.-H. Kuo, et al., "Mitochondrial ROS-Induced ERK1/2 Activation and HSF2-Mediated AT1R Upregulation Are Required for Doxorubicin-Induced Cardiotoxicity," *Journal of Cellular Physiology* 233, no. 1 (2018): 463–475, <https://doi.org/10.1002/jcp.25905>.

7. G. Napolitano, G. Fasciolo, and P. Venditti, "Mitochondrial Management of Reactive Oxygen Species," *Antioxidants* 10, no. 11 (2021): 1824, <https://doi.org/10.3390/antiox10111824>.

8. A. H. Schapira, "Mitochondria in the Aetiology and Pathogenesis of Parkinson's Disease," *The Lancet Neurology* 7, no. 1 (2008): 97–109, [https://doi.org/10.1016/S1474-4422\(07\)70327-7](https://doi.org/10.1016/S1474-4422(07)70327-7).

9. N. Exner, A. K. Lutz, C. Haass, and K. F. Winklhofer, "Mitochondrial Dysfunction in Parkinson's Disease: Molecular Mechanisms and Pathophysiological Consequences," *The EMBO Journal* 31, no. 14 (2012): 3038–3062, <https://doi.org/10.1038/emboj.2012.170>.

10. B. A. Kaufman, N. Durisic, J. M. Mativetsky, et al., "The Mitochondrial Transcription Factor TFAM Coordinates the Assembly of Multiple DNA Molecules into Nucleoid-like Structures," *Molecular Biology of the Cell* 18, no. 9 (2007): 3225–3236, <https://doi.org/10.1091/mbc.e07-05-0404>.

11. A. Picca and A. M. S. Lezza, "Regulation of Mitochondrial Biogenesis through TFAM–Mitochondrial DNA Interactions," *Mitochondrion* 25 (2015): 67–75, <https://doi.org/10.1016/j.mito.2015.10.001>.

12. A. Picca, R. Calvani, C.-J. HJ, F. Landi, R. Bernabei, and E. Marzetti, "Mitochondrial Dysfunction, Oxidative Stress, and Neuroinflammation: Intertwined Roads to Neurodegeneration," *Antioxidants* 9, no. 8 (2020): 647, <https://doi.org/10.3390/antiox9080647>.

13. Y.-T. Hsieh, H.-F. Tu, M.-H. Yang, et al., "Mitochondrial Genome and Its Regulator TFAM Modulates Head and Neck Tumorigenesis through Intracellular Metabolic Reprogramming and Activation of Oncogenic Effectors," *Cell Death & Disease* 12, no. 11 (2021): 961, <https://doi.org/10.1038/s41419-021-04255-w>.

14. S. Anilkumar and E. Wright-Jin, "NF- κ B as an Inducible Regulator of Inflammation in the Central Nervous System," *Cells* 13, no. 6 (2024): 485, <https://doi.org/10.3390/cells13060485>.

15. M. T. Jacques, L. Saso, and M. Farina, "LPS-Activated Microglial Cell-Derived Conditioned Medium Protects HT22 Neuronal Cells against Glutamate-Induced Ferroptosis," *International Journal of Molecular Sciences* 24, no. 3 (2023): 2910, <https://doi.org/10.3390/ijms24032910>.

16. C. Böröczky, A. Paszternák, R. Laufer, et al., "Neuroinflammation Based Neurodegenerative in Vitro Model of SH-SY5Y Cells—Differential Effects on Oxidative Stress and Insulin Resistance Relevant to Alzheimer's Pathology," *International Journal of Molecular Sciences* 26, no. 14 (2025): 6581, <https://doi.org/10.3390/ijms26146581>.

17. H. Tirichen, H. Yaigoub, W. Xu, C. Wu, R. Li, and Y. Li, "Mitochondrial Reactive Oxygen Species and Their Contribution in Chronic Kidney Disease Progression through Oxidative Stress," *Frontiers in Physiology* 12 (2021): 627837, <https://doi.org/10.3389/fphys.2021.627837>.

18. S. Sunilkumar, A. M. VanCleave, C. M. McCurry, et al., "REDD1-dependent GSK3 β Dephosphorylation Promotes NF- κ B Activation and

- Macrophage Infiltration in the Retina of Diabetic Mice,” *Journal of Biological Chemistry* 299, no. 8 (2023): 104991, <https://doi.org/10.1016/j.jbc.2023.104991>.
19. G. Lei, Y. Xia, and K. M. Johnson, “The Role of Akt-GSK-3 β Signaling and Synaptic Strength in Phencyclidine-Induced Neurodegeneration,” *Neuropsychopharmacology* 33, no. 6 (2008): 1343–1353, <https://doi.org/10.1038/sj.npp.1301511>.
20. A. A. Singh, S. Katiyar, and M. Song, “Phytochemicals Targeting BDNF Signaling for Treating Neurological Disorders,” *Brain Sciences* 15, no. 3 (2025): 252, <https://doi.org/10.3390/brainsci15030252>.
21. S. C. Badoiu, M. Greabu, D. Miricescu, et al., “PI3K/AKT/mTOR Dysregulation and Reprogramming Metabolic Pathways in Renal Cancer: Crosstalk with the VHL/HIF Axis,” *International Journal of Molecular Sciences* 24, no. 9 (2023): 8391, <https://doi.org/10.3390/ijms24098391>.
22. H. Albert-Gascó, F. Ros-Bernal, E. Castillo-Gómez, and F. E. Olucha-Bordonau, “MAP/ERK Signaling in Developing Cognitive and Emotional Function and Its Effect on Pathological and Neurodegenerative Processes,” *International Journal of Molecular Sciences* 21, no. 12 (2020): 4471, <https://doi.org/10.3390/ijms21124471>.
23. Z. Li, J. Carter, L. Santos, et al., “Acidification-Induced Structure Evolution of Lipid Nanoparticles Correlates with Their in Vitro Gene Transfections,” *ACS Nano* 17, no. 2 (2023): 979–990, <https://doi.org/10.1021/acsnano.2c06213>.
24. T. Akanchise, F. Luo, B. Angelov, Y. Deng, G. Manna, and A. Angelova, “Rapid Structural Transformation of Ionizable Lipid Nanoparticles Involving Omega-3 Polyunsaturated Fatty Acids Enhances Antioxidant Defense and Mitochondrial Proteins Activity in pH-responsive Drug Delivery,” *Journal of Colloid and Interface Science* 704 (2026): 139420, <https://doi.org/10.1016/j.jcis.2025.139420>.
25. J. Philipp, A. Dabkowska, A. Reiser, et al., “pH-dependent Structural Transitions in Cationic Ionizable Lipid Mesophases Are Critical for Lipid Nanoparticle Function,” *Proceedings of the National Academy of Sciences* 120, no. 50 (2023): 2310491120, <https://doi.org/10.1073/pnas.2310491120>.
26. Z. Ma, H. A. Dang, J. Yang, et al., “Lipid Nanoparticle-mediated Delivery of microRNA-124 Reduces Neuroinflammation,” *Biomaterials* 325 (2026): 123589, <https://doi.org/10.1016/j.biomaterials.2025.123589>.
27. H. Xiao, O. Amarsaikhan, Y. Zhao, et al., “Astrocyte-targeted siRNA Delivery by Adenosine-functionalized LNP in Mouse TBI Model,” *Molecular Therapy Nucleic Acids* 34 (2023): 102065, <https://doi.org/10.1016/j.omtn.2023.102065>.
28. D. Cao, X. Hou, C. Wang, et al., “Lipid Nanoparticles for mRNA Delivery in Brain via Systemic Administration,” *Science Advances* 11, no. 33 (2025), <https://doi.org/10.1126/sciadv.adw0730>.
29. A. Biscans, S. Ly, N. McHugh, D. A. Cooper, and A. Khvorova, “Engineered Ionizable Lipid siRNA Conjugates Enhance Endosomal Escape but Induce Toxicity in Vivo,” *Journal of Controlled Release* 349 (2022): 831–843, <https://doi.org/10.1016/j.jconrel.2022.07.041>.
30. O. Escalona-Rayó, Y. Zeng, R. A. Knol, et al., “In Vitro and in Vivo Evaluation of Clinically-approved Ionizable Cationic Lipids Shows Divergent Results between mRNA Transfection and Vaccine Efficacy,” *Biomedicine & Pharmacotherapy* 165 (2023): 115065, <https://doi.org/10.1016/j.biopha.2023.115065>.
31. M. Jayaraman, S. M. Ansell, B. L. Mui, et al., “Maximizing the Potency of siRNA Lipid Nanoparticles for Hepatic Gene Silencing in Vivo**,” *Angewandte Chemie International Edition* 51, no. 34 (2012): 8529–8533, <https://doi.org/10.1002/anie.201203263>.
32. J. D. Quick, C. Silva, J. H. Wong, et al., “Lysosomal Acidification Dysfunction in Microglia: an Emerging Pathogenic Mechanism of Neuroinflammation and Neurodegeneration,” *Journal of Neuroinflammation* 20, no. 1 (2023): 185, <https://doi.org/10.1186/s12974-023-02866-y>.
33. C. H. Lo and J. Zeng, “Defective Lysosomal Acidification: a New Prognostic Marker and Therapeutic Target for Neurodegenerative Diseases,” *Translational Neurodegeneration* 12, no. 1 (2023): 29, <https://doi.org/10.1186/s40035-023-00362-0>.
34. H. Hagihara and T. Miyakawa, “Decreased Brain pH Correlated with Progression of Alzheimer Disease Neuropathology: a Systematic Review and Meta-Analyses of Postmortem Studies,” *International Journal of Neuropsychopharmacology* 27, no. 10 (2024): pyae047, <https://doi.org/10.1093/ijnp/pyae047>.
35. X. Wang, X. Shao, L. Yu, et al., “Changes in the pH Value of the Human Brain in Alzheimer’s Disease Pathology Correlated with CD68-Positive Microglia: a Community-Based Autopsy Study in Beijing, China,” *Molecular Brain* 18, no. 1 (2025): 10, <https://doi.org/10.1186/s13041-025-01180-3>.
36. A. Picca, R. Calvani, H.-J. Coelho-Junior, F. Landi, R. Bernabei, and E. Marzetti, “Mitochondrial Dysfunction, Oxidative Stress, and Neuroinflammation: Intertwined Roads to Neurodegeneration,” *Antioxidants* 9, no. 8 (2020): 647, <https://doi.org/10.3390/antiox9080647>.
37. X. Cheng, C. Peuckert, and S. Wölfl, “Essential Role of Mitochondrial Stat3 in p38MAPK Mediated Apoptosis under Oxidative Stress,” *Scientific Reports* 7, no. 1 (2017): 15388, <https://doi.org/10.1038/s41598-017-15342-4>.
38. J. M. Grimes and K. V. Grimes, “p38 MAPK Inhibition: a Promising Therapeutic Approach for COVID-19,” *Journal of Molecular and Cellular Cardiology* 144 (2020): 63–65, <https://doi.org/10.1016/j.yjmcc.2020.05.007>.
39. M. J. Chen, S. Ramesha, L. D. Weinstock, et al., “Extracellular Signal-Regulated Kinase Regulates Microglial Immune Responses in Alzheimer’s Disease,” *Journal of Neuroscience Research* 99, no. 6 (2021): 1704–1721, <https://doi.org/10.1002/jnr.24829>.
40. D. Galter, K. Pernold, T. Yoshitake, et al., “MitoPark Mice Mirror the Slow Progression of Key Symptoms and L-DOPA Response in Parkinson’s Disease,” *Genes, Brain and Behavior* 9, no. 2 (2010): 173–181, <https://doi.org/10.1111/j.1601-183X.2009.00542.x>.
41. J. Prasuhn, R. L. Davis, and K. R. Kumar, “Targeting Mitochondrial Impairment in Parkinson’s Disease: Challenges and Opportunities,” *Frontiers in Cell and Developmental Biology* 8 (2021): 615461, <https://doi.org/10.3389/fcell.2020.615461>.
42. M. Abrishamdar, M. S. Jalali, and Y. Farbood, “Targeting Mitochondria as a Therapeutic Approach for Parkinson’s Disease,” *Cellular and Molecular Neurobiology* 43, no. 4 (2023): 1499–1518, <https://doi.org/10.1007/s10571-022-01265-w>.
43. L. Zheng, S. R. Bandara, Z. Tan, and C. Leal, “Lipid Nanoparticle Topology Regulates Endosomal Escape and Delivery of RNA to the Cytoplasm,” *Proceedings of the National Academy of Sciences* 120, no. 27 (2023): 2301067120, <https://doi.org/10.1073/pnas.2301067120>.
44. O. Mertins, P. D. Mathews, and A. Angelova, “Advances in the Design of pH-Sensitive Cubosome Liquid Crystalline Nanocarriers for Drug Delivery Applications,” *Nanomaterials* 10, no. 5 (2020): 963, <https://doi.org/10.3390/nano10050963>.
45. C. F. Holder and R. E. Schaak, “Tutorial on Powder X-ray Diffraction for Characterizing Nanoscale Materials,” *ACS Nano* 13, no. 7 (2019): 7359–7365, <https://doi.org/10.1021/acsnano.9b05157>.
46. A. Yaghmur and O. Glatter, “Characterization and Potential Applications of Nanostructured Aqueous Dispersions,” *Advances in Colloid and Interface Science* 147–148 (2009): 333–342, <https://doi.org/10.1016/j.cis.2008.07.007>.
47. J. Rejman, V. Oberle, I. S. Zuhorn, and D. Hoekstra, “Size-dependent Internalization of Particles via the Pathways of Clathrin- and Caveolae-mediated Endocytosis,” *Biochemical Journal* 377, no. 1 (2004): 159–169, <https://doi.org/10.1042/bj20031253>.
48. M. Danaei, M. Dehghankhold, S. Ataei, et al., “Impact of Particle Size and Polydispersity Index on the Clinical Applications of Lipidic Nanocarrier Systems,” *Pharmaceutics* 10, no. 2 (2018): 57, <https://doi.org/10.3390/pharmaceutics10020057>.
49. T. Akanchise and A. Angelova, “Ginkgo Biloba and Long COVID: in Vivo and in Vitro Models for the Evaluation of Nanotherapeutic Efficacy,” *Pharmaceutics* 15, no. 5 (2023): 1562, <https://doi.org/10.3390/pharmaceutics15051562>.

50. A. T. Dinkova-Kostova, R. V. Kostov, and A. G. Kazantsev, "The Role of Nrf2 Signaling in Counteracting Neurodegenerative Diseases," *The FEBS Journal* 285, no. 19 (2018): 3576–3590, <https://doi.org/10.1111/febs.14379>.
51. E. Kansanen, S. M. Kuosmanen, H. Leinonen, and A. L. Levenon, "The Keap1-Nrf2 Pathway: Mechanisms of Activation and Dysregulation in Cancer," *Redox Biology* 1, no. 1 (2013): 45–49, <https://doi.org/10.1016/j.redox.2012.10.001>.
52. S. M. U. Ahmed, L. Luo, A. Namani, X. J. Wang, and X. Tang, "Nrf2 signaling Pathway: Pivotal Roles in Inflammation," *Biochimica et Biophysica Acta (BBA)—Molecular Basis of Disease* 1863, no. 2 (2017): 585–597, <https://doi.org/10.1016/j.bbadis.2016.11.005>.
53. A. K. Aranda-Rivera, A. Cruz-Gregorio, J. Pedraza-Chaverri, and A. Scholze, "Nrf2 Activation in Chronic Kidney Disease: Promises and Pitfalls," *Antioxidants* 11, no. 6 (2022): 1112, <https://doi.org/10.3390/antiox11061112>.
54. L. Baird and M. Yamamoto, "The Molecular Mechanisms Regulating the KEAP1-NRF2 Pathway," *Molecular and Cellular Biology* 40, no. 13 (2020), <https://doi.org/10.1128/MCB.00099-20>.
55. A. A. Bhat, E. Moglad, A. Goyal, et al., "Nrf2 pathways in Neuroprotection: Alleviating Mitochondrial Dysfunction and Cognitive Impairment in Aging," *Life Sciences* 357 (2024): 123056, <https://doi.org/10.1016/j.lfs.2024.123056>.
56. C.-C. Yang, L.-D. Hsiao, C.-Y. Wang, et al., "HO-1 Upregulation by Kaempferol via ROS-Dependent Nrf2-ARE Cascade Attenuates Lipopolysaccharide-Mediated Intercellular Cell Adhesion Molecule-1 Expression in Human Pulmonary Alveolar Epithelial Cells," *Antioxidants* 11, no. 4 (2022): 782, <https://doi.org/10.3390/antiox11040782>.
57. T. Akanchise, B. Angelov, and A. Angelova, "Nanomedicine-Mediated Recovery of Antioxidant Glutathione Peroxidase Activity after Oxidative-Stress Cellular Damage: Insights for Neurological Long COVID," *Journal of Medical Virology* 96, no. 5 (2024): 29680, <https://doi.org/10.1002/jmv.29680>.
58. T. Narayanan, M. Sztucki, P. Van Vaerenbergh, et al., "A Multipurpose Instrument for Time-resolved Ultra-small-angle and Coherent X-ray Scattering," *Journal of Applied Crystallography* 51, no. 6 (2018): 1511–1524, <https://doi.org/10.1107/S1600576718012748>.
59. T. Narayanan, M. Sztucki, T. Zinn, et al., "Performance of the Time-resolved Ultra-small-angle X-ray Scattering Beamline with the Extremely Brilliant Source," *Journal of Applied Crystallography* 55, no. 1 (2022): 98–111, <https://doi.org/10.1107/S1600576721012693>.
60. L. Matthews and T. Narayanan, "High-resolution Structural Elucidation of Extremely Swollen Lyotropic Phases," *Journal of Colloid and Interface Science* 610 (2022): 359–367, <https://doi.org/10.1016/j.jcis.2021.11.168>.
61. H. Yu, A. Angelova, B. Angelov, et al., "Real-Time pH-Dependent Self-Assembly of Ionisable Lipids from COVID-19 Vaccines and in Situ Nucleic Acid Complexation," *Angewandte Chemie* 135, no. 35 (2023): 202304977, <https://doi.org/10.1002/ange.202304977>.
62. M. Rakotoarisoa, B. Angelov, S. Espinoza, et al., "Composition-Switchable Liquid Crystalline Nanostructures as Green Formulations of Curcumin and Fish Oil," *ACS Sustainable Chemistry & Engineering* 9, no. 44, (2021): 14821–14835, <https://doi.org/10.1021/acssuschemeng.1c04706>.
63. T. Akanchise, B. Angelov, Y. Deng, T. Fujino, T. Bizien, and A. Angelova, "Nanostructuring and Antioxidant Activity of Nanotherapeutics Designed by Self-Assembly of Natural Lipids and Phytochemicals," *ACS Biomaterials Science & Engineering* 11 (2025): 3488–3502, <https://doi.org/10.1021/acsbomaterials.5c00006>.

Supporting Information

Additional supporting information can be found online in the Supporting Information section.

Supporting File: adhm71127-sup-0001-SuppMat.pdf.